

AFOSR SUMMARY SCIENTIFIC REPORT 68-0489

ON

AD 669836

RESEARCH ON ENERGY ABSORBING STRUCTURES,
PART VI

Contract Number: AF 49(638)-1521

Prepared for

Air Force Office of Scientific Research (OAR)

Arlington, Virginia 22209

D D C
RECEIVED
JUN 5 1968
RECEIVED
C



AEROSPACE RESEARCH ASSOCIATES

2017 West Garvey Avenue • West Covina, California • Tel. 962-1045

MARCH 1968

Reproduced by the
CLEARINGHOUSE
for Federal Scientific & Technical
Information Springfield Va. 22151

1. This document has been approved for public
release and sale; its distribution is unlimited.

**Annual Report on Research on
Energy Absorbing Structures
Part VI**

Contract Number: AF 49(638)-1521

ARA Report No. 94

**Prepared for
Air Force Office of Scientific Research
Arlington, Virginia 22209**

March 1968

FOREWORD

The research work described in this report was performed by ARA, Inc., West Covina, California, for the Mechanics Division, Directorate of Engineering Services, Air Force Office of Scientific Research, Arlington, Virginia 22209, under Contract Number AF 49(638)-1521. This research represents the sixth-year program and is part of a continuing effort in the study of variable geometry energy absorbing structures. The Project-Task No. is 9782-01. The Project Engineer was Dr. Jacob Pomerantz.

The studies presented began 1 February 1967 and were concluded 31 January 1968. Mr. Bernard Maze!sky, President of ARA, Inc., was the Program Manager.

Other ARA, Inc. personnel who participated in this program were: Analytical and experimental effort - Mr. S. R. Lin and Mr. Chi-Kung Yu. Dr. T. H. Lin, Professor of Engineering, UCLA, served as a Consultant on the analytical study.

TABLE OF CONTENTS

	<u>Page</u>
Part A - Large Inextensional Deflection of Thin Cantilevered Plates	1
I SUMMARY	1
II INTRODUCTION	1
III MANSFIELD AND KLEEMAN'S INEXTENSIONAL THEORY OF PLATES	2
IV MOMENT ARM OF DEFLECTED PLATE	5
V CALCULATION OF LARGE DEFLECTIONS BY METHOD OF VIRTUAL WORK	6
VI EXPERIMENTAL TEST	13
VII CONCLUSION	17
Part B - Effect of Bi-Axial Stresses On Low Cycle Fatigue	19
I SUMMARY AND INTRODUCTION	19
II EXPERIMENTAL TEST SET-UP OF LOW CYCLE TORSION TESTER	20
A. Calibration	27
III TEST SPECIMENS	28
IV TEST RESULTS	28
A. Aluminum Alloy	30
B. Beryllium Copper	30
V DISCUSSION AND CONCLUDING REMARKS	44
A. Correlation of Data with Coffin's Equation	44
B. Effect of Axial Stress on Fatigue and Absorbed Energy	45
C. Effects Due to Work Hardening	45

TABLE OF CONTENTS (Continued)

	<u>Page</u>
D. Effect of Cyclic Torsion Strain on Axial Strain	53
E. Some Analytical Considerations	53
VI REFERENCES	59

LIST OF FIGURES

<u>Figure</u>		<u>Page</u>
1	Generators of a Cantilevered Plate	3
2	A Cantilever Square Plate Subjected to Concentrated Load P at "A"	8
3	Deflection Curve of the Leading Edge at Different Loads	14
4	Tip Deflection Versus Applied Load	15
5	Schematic of Bi-Axial Cyclic Torsion Test Apparatus	21
6	Close-Up View of Cyclic Torsion Apparatus	22
7	Close-Up View of Recording Equipment For Cyclic Torsion Apparatus	23
8	View of Axial Tension-Compression Beam and Deflection Recording Technique For Cyclic Torsion Apparatus	24
9	Close-Up View of Axial Load Bearing Housing For Cyclic Torsion Apparatus	25
10	Typical Specimen Dimensions	29
11	Cyclic Torsion Fatigue Curve for Aluminum Alloy 2024 T4	34
12	Effect of Axial Stress on Cyclic Torsion Fatigue Failure of Aluminum Alloy 2024 T351 With 3% Total Shear Strain	35
13	Effect of Axial Stress on Cyclic Torsion Fatigue Failure of Aluminum Alloy 2024 T351 With 4% Total Shear Strain	36
14	Variation of Total Energy Dissipated In Cyclic Torsion at 3% Total Shear Strain With Axial Load for Aluminum Alloy 2024 T351	37
15	Variation of Total Energy Dissipated in Cyclic Torsion at 4% Total Shear Strain With Axial Load for Aluminum Alloy 2024 T351	38
16	Cyclic Torsion Fatigue Curve for Beryllium Copper	39
17	Effect of Axial Stress on Cyclic Torsion Fatigue Failure of Beryllium Copper With 3% Total Shear Strain	40
18	Effect of Axial Stress on Cyclic Torsion Fatigue Failure of Beryllium Copper With 4.5% Total Shear Strain	41

LIST OF FIGURES (Continued)

<u>Figure</u>		<u>Page</u>
19	Variation of Total Energy Dissipated in Cyclic Torsion at 3% Total Shear Strain With Axial Load For Beryllium Copper	42
20	Variation of Total Energy Dissipated in Cyclic Torsion at 4.5% Total Shear Strain With Axial Load For Beryllium Copper	43
21	Typical Changes of Maximum Shear Stress and Energy Dissipated Due to Cyclic Torsion For Aluminum Alloy 2024 T351 at 4% Total Shear Strain	47
22	Typical Changes of Maximum Shear Stress and Axial Deflection Due to Cyclic Torsion for Aluminum Alloy 2024 T351 at 3% Total Shear Strain and 20,000 psi Axial Compression	48
23	Typical Changes of Maximum Shear Stress and Axial Deflection Due to Cyclic Torsion for Aluminum Alloy 2024 T351 at 4% Total Shear Strain and 20,000 psi Axial Compression	49
24	Typical Changes of Maximum Shear Stress and Energy Dissipated Due to Cyclic Torsion for Beryllium Copper at 3% Total Shear Strain	50
25	Typical Changes of Maximum Shear Stress and Axial Deflection Due to Cyclic Torsion for Beryllium Copper at 3% Total Shear Strain and 20,000 psi Axial Compression	51
26	Typical Changes of Maximum Shear Strain and Axial Deflection Due to Cyclic Torsion for Beryllium Copper at 3% Total Shear Strain and 30,000 psi Axial Compression	52
27	Variation of Fatigue Stress With Plastic Strain Range for Al 2024 T4	55
28	Variation of Fatigue Stress With Plastic Strain Range For Beryllium Copper	56
29	Variation of Total Energy Dissipated Due to Cyclic Torsion With Plastic Strain Range For Aluminum Alloy 2024 T4	58

LIST OF TABLES

<u>Table</u>		<u>Page</u>
I	Mechanical Properties of Test Specimens	28
II	Cyclic Torsion Tests for Al 2024 T4	31
	Cyclic Torsion Tests for Al 2024 T351	32
	Cyclic Torsion Tests for Beryllium Copper 25	33

Part A

Large Inextensional Deflection of Thin Cantilevered Plates

I SUMMARY

The calculation of large bending deflections of thin plates by available techniques are either too difficult to use or are limited to deflections which are below 20% of the plate's length and/or width. The present method predicts, and is substantiated by experiment, the maximum deflections of such thin plates within a few percent wherein the deflections are larger than half the length and/or width of the thin plate.

II INTRODUCTION

The small deflection theory of plates is generally considered to be valid for deflections which are small in comparison with the plate thickness¹. For deflections larger than the plate thickness, Von Karman² has shown an exact large deflection theory in two non-linear differential equations. However, these equations are extremely difficult to use. When the loading is resisted primarily by the flexural rigidity of the plate, Mansfield and Kleeman^{3,4} have proposed an inextensional large deflection theory which assumes the middle surface of the plate to be inextensional. This does not introduce much error for cantilevered thin plates where

the extensional rigidity is large in comparison with the flexural rigidity. The validity of this inextensional theory has been established by correlation with experiment for deflections many times the plate thickness and from comparisons with known theoretical solutions of some simple plate problems. This theory predicts the proportionality of the deflection to the load for any given type of load, and does not consider the effect of the change of geometry on the bending moment. Hence, when the deflection becomes the same magnitude as the linear dimension of the plate, this theory is expected to be inadequate. The present paper describes a method which accounts for this change of geometry in the bending moment, so as to extend Mansfield and Kleeman's inextensional theory to very large deflections, i.e., those having the same magnitude as the width or length of the plate.

III MANSFIELD AND KLEEMAN'S INEXTENSIONAL THEORY OF PLATES

For later reference, the inextensional theory of Mansfield and Kleeman is first briefly reviewed. Since the middle surface of the plate is inextensional, it must be a developable surface, so the problem is to determine the generators of this surface. Consider a cantilever plate as shown in Figure 1 with x-axis normal to the fixed boundary of the plate. The intersection of the two generators mn and m'n' at H generate angles α and $\alpha + d\alpha$ at the x-axis. The strip element mn n' m' forms part of a conical surface with apex at H.

From geometry

$$\eta_x = \frac{dx}{d\alpha} \sin \alpha \quad (1)$$

where η_x is the distance along the generator from the apex H to the x-axis.

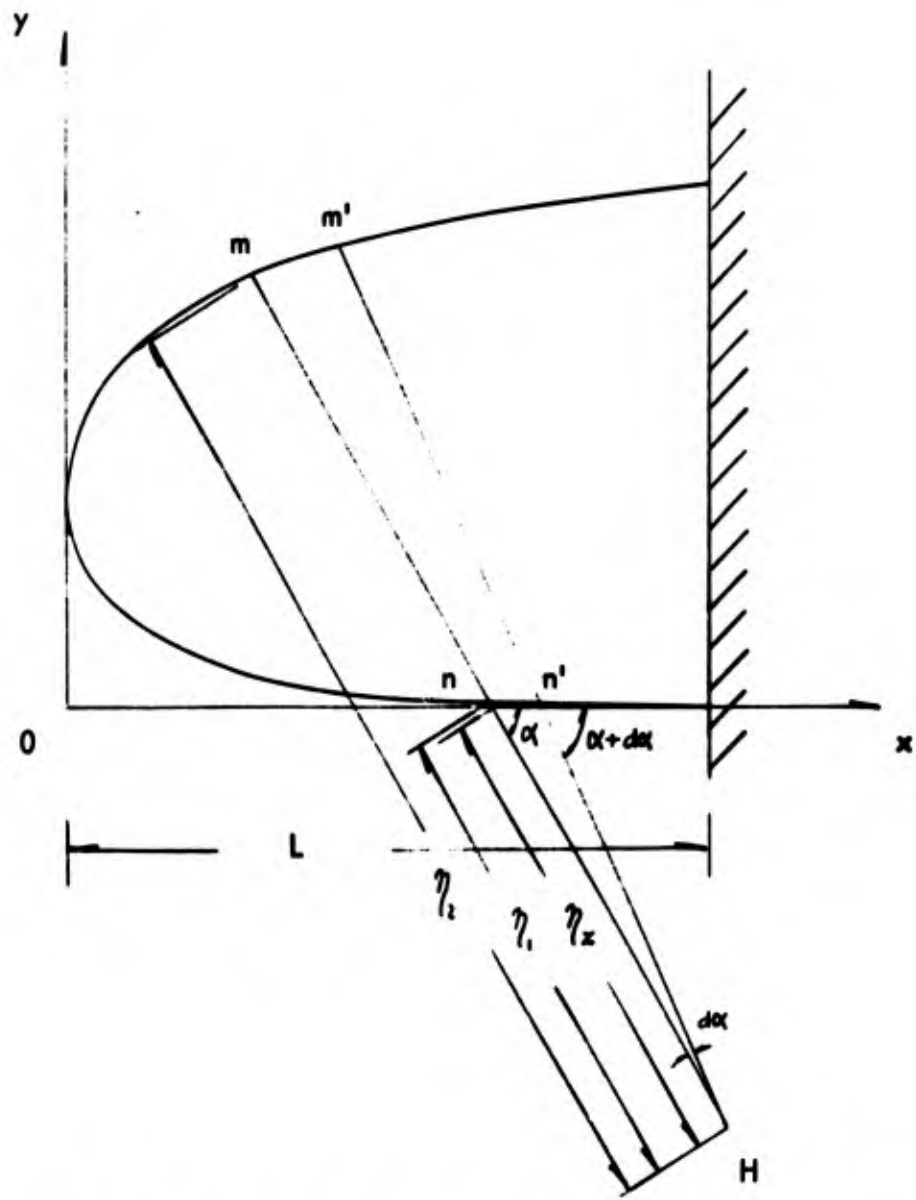


Fig. 1 Generators of a Cantilevered Plate

Let M_η be the moment per unit length about the generator, and D_η the flexural rigidity of the plate at η along the generator. η_1 and η_2 are denoted by η_1 and η_2 respectively. Then

$$\frac{M_\eta}{D_\eta} = \frac{1}{r_\eta} \quad (2)$$

where r_η is the radius of curvature at η . From the conical properties of the strip,

$$\frac{\eta M_\eta}{D_\eta} = c \quad (3)$$

where c is a constant.

The resisting moment about the generator is

$$\int_{\eta_1}^{\eta_2} M_\eta d\eta = c \int_{\eta_1}^{\eta_2} \frac{D_\eta}{\eta} d\eta \quad (4)$$

This must be equal to the applied moment $M(\alpha)$ about the generator. The strain energy is

$$\begin{aligned} U &= \frac{1}{2} \int \int_{\eta_1}^{\eta_2} \frac{M_\eta^2}{D_\eta} \eta d\eta d\alpha \\ &= \frac{1}{2} \int (M^2(\alpha) / \int_{\eta_1}^{\eta_2} \frac{D_\eta}{\eta} d\eta) d\alpha \end{aligned} \quad (5)$$

For a given loading,

$$U = \frac{1}{2} \int F(\alpha, x, x') d\alpha \quad (6)$$

where the prime denotes differentiation with respect to α . The variation of α

with x is determined from the condition that U is a maximum. The condition to extremize the integral gives

$$x'' F_{x'x'} + x' F_{xx'} + F_{\alpha x'} - F_x = 0 \quad (7)$$

From Equation (7), the variation of α with x is determined.

IV MOMENT ARM OF DEFLECTED PLATE

The original Mansfield and Kleeman's theory is applicable for deflections many times the thickness but are small when compared to the other linear dimensions of the plate. The theory does not account for the change in the moment arm of the load due to large plate deflections. When the vertical deflection of the plate reaches the same order of magnitude of its length, the change in the moment arm becomes appreciable and must be considered. Let the z -axis be along the vertical direction and the y -axis be normal to both the x and z axes. Since the deformation is inextensional, an elemental length Δx in the plate before bending will retain the same length in the deflected surface, but will have projections along the three axes $\Delta \bar{x}$, $\Delta \bar{y}$, and $\Delta \bar{z}$, after bending. On this basis,

$$\Delta \bar{x} = \sqrt{(\Delta x)^2 - (\Delta \bar{y})^2 - (\Delta \bar{z})^2} \quad (8)$$

For a number of cases, $\Delta \bar{y}$ is small as compared to $\Delta \bar{z}$, then $\Delta \bar{y}$ may be neglected without introducing a large error. Thus

$$\Delta \bar{x} \cong \sqrt{(\Delta x)^2 - (\Delta \bar{z})^2} \quad (9)$$

For such cases, the calculation of the moment arm in the deflected shape reduces to the calculation of vertical deflections \bar{z} 's at different points along the x-axis.

V CALCULATION OF LARGE DEFLECTIONS BY METHOD OF VIRTUAL WORK

Slope and deflections of beams of small deformation have been commonly calculated by the method of virtual work. In this method, a fictitious unit load is placed at a point along the direction in which the deflection is to be determined.

Consider a thin cantilever plate; let $m_B(\alpha)$ denote the bending moment in the plate at generator angle α due to a vertical unit load applied at B. Neglecting the change of moment arm, $M(\alpha)$ is proportional to P , and $m_B(\alpha)$ is independent of P . When the deflection becomes large and the change of moment arm is considered, $M(\alpha)$ and $m_B(\alpha)$ both may vary non-linearly with P and are written as $M(\alpha, P)$ and $m_B(\alpha, P)$. For $d\alpha$ of the plate, the change of slope for an incremental load dP is

$$d\theta = \frac{1}{D \ln \frac{\gamma_2}{\gamma_1}} \frac{\partial M(\alpha, P)}{\partial P} dP d\alpha \quad (10)$$

The virtual work done by $m_B(\alpha, P)$ is then

$$m_B(\alpha, P) d\theta = \frac{m_B(\alpha, P)}{D \ln \frac{\gamma_2}{\gamma_1}} \frac{\partial M(\alpha, P)}{\partial P} dP d\alpha \quad (11)$$

The total internal work done in the plate by $m_B(\alpha, P)$ during loading from zero to P equals

$$\int_{\alpha_0}^{\alpha_L} \int_0^P \frac{m_B(\alpha, P)}{D \ln \frac{\eta_2}{\eta_1}} \frac{\partial M(\alpha, P)}{\partial P} dP d\alpha \quad (12)$$

where α_0 and α_L are the generator angles at $x = 0$ and $x = L$ respectively.

This work must be equal to the external work done by the fictitious unit load applied at B:

$$1 \times z_B = \int_{\alpha_0}^{\alpha_L} \int_0^P \frac{m_B(\alpha, P)}{D \ln \frac{\eta_2}{\eta_1}} \frac{\partial M(\alpha, P)}{\partial P} dP d\alpha \quad (13)$$

When the change of moment arm is not considered, the above equation reduces to the following commonly used virtual work expressions for displacement as

$$1 \times z_B = \int_{\alpha_0}^{\alpha_L} \frac{m_B(\alpha, P) M(\alpha)}{D \ln \frac{\eta_2}{\eta_1}} d\alpha \quad (14)$$

The calculation of vertical deflection considering the change in moment arm by Equation (13) is illustrated by the following example:

Consider a cantilevered thin plate of beryllium copper as shown in Figure 2 with the dimensions 6" x 6" x .0194" which is subjected to a concentrated load P normal to the plate at one end of the free corners (Point A). The Young's modulus is 18.5×10^6 lb/in² and the flexural rigidity is $D = 12.38$ lb-in.

Along AN, $\alpha \leq \alpha_1$

$$\eta_2 = \eta_1 + \frac{x}{\cos \alpha} \quad (15)$$

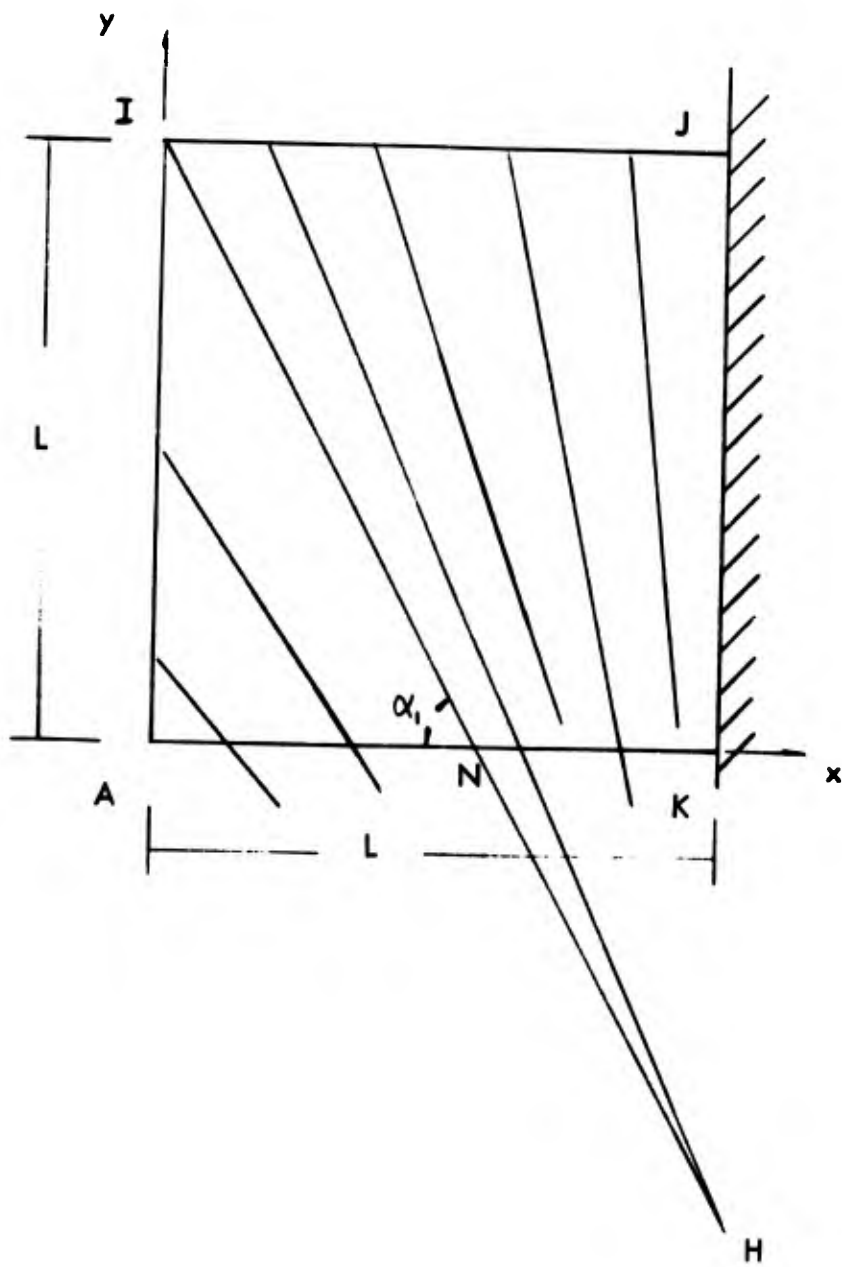


Fig. 2 A Cantilever Square Plate Subjected to Concentrated Load P at "A"

$$F = F_1 = \frac{P^2}{D} \left[\frac{x^2 \sin^2 \alpha}{\ln \left(1 + \frac{2x}{x' \sin 2\alpha} \right)} \right] \quad (16)$$

Along NK, $\alpha \geq \alpha_1$,

$$\eta_2 = \eta_1 + \frac{L}{\sin \alpha} \quad (17)$$

$$F = F_2 = \frac{P^2}{D} \left[\frac{x^2 \sin^2 \alpha}{\ln \left(1 + \frac{L}{x' \sin^2 \alpha} \right)} \right] \quad (18)$$

The total strain energy is

$$U = \frac{1}{2} \left[\int_{\alpha_0}^{\alpha_1} F_1(\alpha, x, x') d\alpha + \int_{\alpha_0}^{\alpha_L} F_2(\alpha, x, x') d\alpha \right] \quad (19)$$

Extremizing this integral by calculus of variations shows that Equation (7) is to be satisfied for both F_1 and F_2 . On both sides of the generator α_1 , $\frac{M_2}{D} = \frac{1}{r_2}$ must be the same along this generator, so η_1 must be continuous across α_1 .

Hence, from Equation (1), x' must be continuous. With this condition and the continuity of α across this generator, together with the conditions $\alpha_0 = 45^\circ$ and $\alpha_L = 90^\circ$, the solution of α versus x was obtained from Equation (7).

Then the integral $\int \frac{(M(\alpha/P))^2}{\ln \frac{\eta_2}{\eta_1}} d\alpha$ over various intervals of α

was determined.

F_1 and F_2 are functions of the applied moments about the different generators. The moment arms about these generators change as the plate deflection reaches the same order of magnitude as the width of the plate. These F_1 and F_2 functions would be extremely complicated to express and to extremize

in terms of the deflections of the plate. Hence, the variation of α versus x which was obtained from extremizing F_1 and F_2 without considering the change of moment arm due to large deflection is assumed to remain the same even when the deflections become $1/5$ to $1/2$ the length of the plate.

From Equation (13)

$$z_{BP_2} - z_{BP_1} = \int_{\alpha_0}^{\alpha_L} \frac{m_B(\alpha, P)}{D \ln \frac{r_2}{r_1}} [M(\alpha, P_2) - M(\alpha, P_1)] d\alpha \quad (20)$$

where z_{BP_1} and z_{BP_2} are deflections at B due to the loading of P_1 and P_2 respectively. Divide $\alpha_L - \alpha_0$ into N intervals of $\Delta\alpha$. Writing the above in a finite difference form:

$$z_{BP_2} - z_{BP_1} = \sum_1^N \frac{m_B(\alpha, P)}{D \ln \frac{r_2}{r_1}} [M(\alpha, P_2) - M(\alpha, P_1)] \Delta\alpha \quad (21)$$

P in $m_B(\alpha, P)$ should lie between P_1 and P_2 . For the following numerical calculation $m_B(\alpha, P_2)$ is used. The deflection increment $(z_{BP_2} - z_{BP_1})$ depends on the values of $m_B(\alpha, P_2)$ and $M(\alpha, P_2)$, which in turn depends on z_{P_2} . For the solution of Equation (21), an iteration procedure is used.

Let the first set of assumed values of $(z_{BP_2} - z_{BP_1})$ be denoted by $(z_{BP_2} - z_{BP_1})_0$. From this set of deflections the moment arms are computed as well as the moments m_B 's and $M(\alpha)$'s together with a set of deflection increments denoted by $(z_{BP_2} - z_{BP_1})_1$. These two sets of deflection increments are averaged to obtain

$$(z_{BP_2} - z_{BP_1})_2 = \frac{1}{2} \left[(z_{BP_2} - z_{BP_1})_0 + (z_{BP_2} - z_{BP_1})_1 \right] \quad (22)$$

The deflection at B under load P_2 at the end of the second iteration is

$$z_{BP_2 2} = z_{BP_1} + (z_{BP_2} - z_{BP_1})_2 \quad (23)$$

Omit the subscript P in the preceding equation with the understanding that the first subscript of z_B denotes the subscript of load P while the second subscript denotes the iteration number. On this basis, the preceding equation becomes

$$z_{B22} = z_{B1} + (z_{B2} - z_{B1})_2 \quad (24)$$

P_1 in this particular calculation is .772 lb which causes a tip deflection of approximately one inch. It is found that at this load, the moment arm change is insignificant. Next consider the load P_2 equal to 1.544 lb where the moment arm change is significant. The term $(z_{B2} - z_{B1})_0$ is taken to be those values obtained by Mansfield and Kleeman's theory. Let \bar{x}_{mn} denote the moment arm of load P at load P_m at nth iteration. Similarly \bar{x}_{Bmn} is the horizontal distance from the loading point to B at load P_m at the nth iteration. Equation (21) can be written as:

$$(z_{B2} - z_{B1})_1 = \sum_{i=1}^N \left\{ \frac{m_{B21}}{D \ln \frac{\eta_2}{\eta_1}} [M(\alpha)_{21} - M(\alpha)_{1f}] \right\}_i \Delta \alpha_i \quad (25)$$

where the subscript "f" denotes the final value of iteration, and

$$\left\{ \begin{array}{l} M(\alpha)_{1f} = \frac{M(\alpha)}{P} \cdot P_1 \\ M(\alpha)_{21} = \frac{M(\alpha)}{P} \cdot P_2 \cdot \frac{\bar{x}_{21}}{x} \\ m_{B_{21}} = \frac{M(\alpha)}{P} \cdot \frac{\bar{x}_{21} - x_{B_{21}}}{x} \end{array} \right. \quad (26)$$

Substituting this result into Equation (25),

$$(z_{B_2} - z_{B_1})_1 = \sum_{i=1}^N \left[\frac{(\bar{x} - \bar{x}_B)_{21}}{x} (P_2 \frac{\bar{x}_{21}}{x} - P_1) \right]_i \times \left\{ \frac{[M(\alpha)/P]^2}{D \ln \frac{r_2}{r_1}} \right\}_i \Delta \alpha_i \quad (27)$$

With initial values of deflections $z_{B_{20}}$ under load P_2 , known, the $\Delta \bar{x}_{21}$ terms are obtained from Equation (9) which in turn determine the \bar{x}_{21} and $\bar{x}_{B_{21}}$ terms. The expressions in the square bracket are readily evaluated.

The terms $\left\{ \frac{[M(\alpha)/P]^2}{D \ln \frac{r_2}{r_1}} \right\}_i \Delta \alpha_i$ were calculated by Mansfield and Kleeman's method. Hence, the right hand of Equation (27) is readily calculated. Then the $z_{B_{22}}$ terms are obtained from Equations (22) and (23). From these deflections, we obtain \bar{x}_{23} and $\bar{x}_{B_{23}}$. The incremental deflection

$$(z_{B_2} - z_{B_1})_3 = \sum_{i=1}^N \left[\frac{(\bar{x} - \bar{x}_B)_{23}}{x} (P_2 \frac{\bar{x}_{23}}{x} - P_1) \right] \frac{[M(\alpha)/P]^2}{D \ln \frac{r_2}{r_1}} \Delta \alpha_i \quad (28)$$

allows for the calculation of terms $z_{B_{23}}$ for the next iteration. This process is repeated until the difference between $(z_{B_2} - z_{B_1})_n$ and $(z_{B_2} - z_{B_1})_{n-1}$ is small. Then the final value of this deflection increment is taken to be

$$(z_{B2} - z_{B1})_f = \frac{1}{2} \left[(z_{B2} - z_{B1})_{n-1} + (z_{B2} - z_{B1})_n \right] \quad (29)$$

When P is increased from P_2 to P_3 , the initial incremental deflection is taken to be

$$(z_{B3} - z_{B2})_0 = \frac{P_3 - P_2}{P_2 - P_1} (z_{B2} - z_{B1})_f \quad (30)$$

and Equation (27) is replaced by

$$(z_{B3} - z_{B2})_i = \sum_{i=1}^N \left[\frac{(\bar{x} - \bar{x}_{B31})}{x} \left(P_3 \frac{\bar{x}_{31}}{x} - P_2 \frac{\bar{x}_{2f}}{x} \right) \right]_i \left\{ \frac{[M(\alpha)/P]^2}{D \ln \frac{r_2}{r_1}} \right\}_i \Delta \alpha_i \quad (31)$$

A similar iteration procedure is utilized. This calculation was performed for the square plate previously described with loads equal to .772, 1.544, 2.650 and 3.970 lbs. The calculated deflection curves at these loads are shown in Figures 3 and 4.

VI EXPERIMENTAL TEST

Experimental deflection data was obtained on the flat plate configuration and loading conditions described in Figure 2. All plate deflections were measured vertically, regardless of the plate deflection amplitudes, as a function of the incrementally increasing corner loads. The plates were fabricated from a six inch by nine inch sheet of Berylco 25 beryllium-copper alloy which was heat treated to the full-hard condition. The nominal sheet thickness

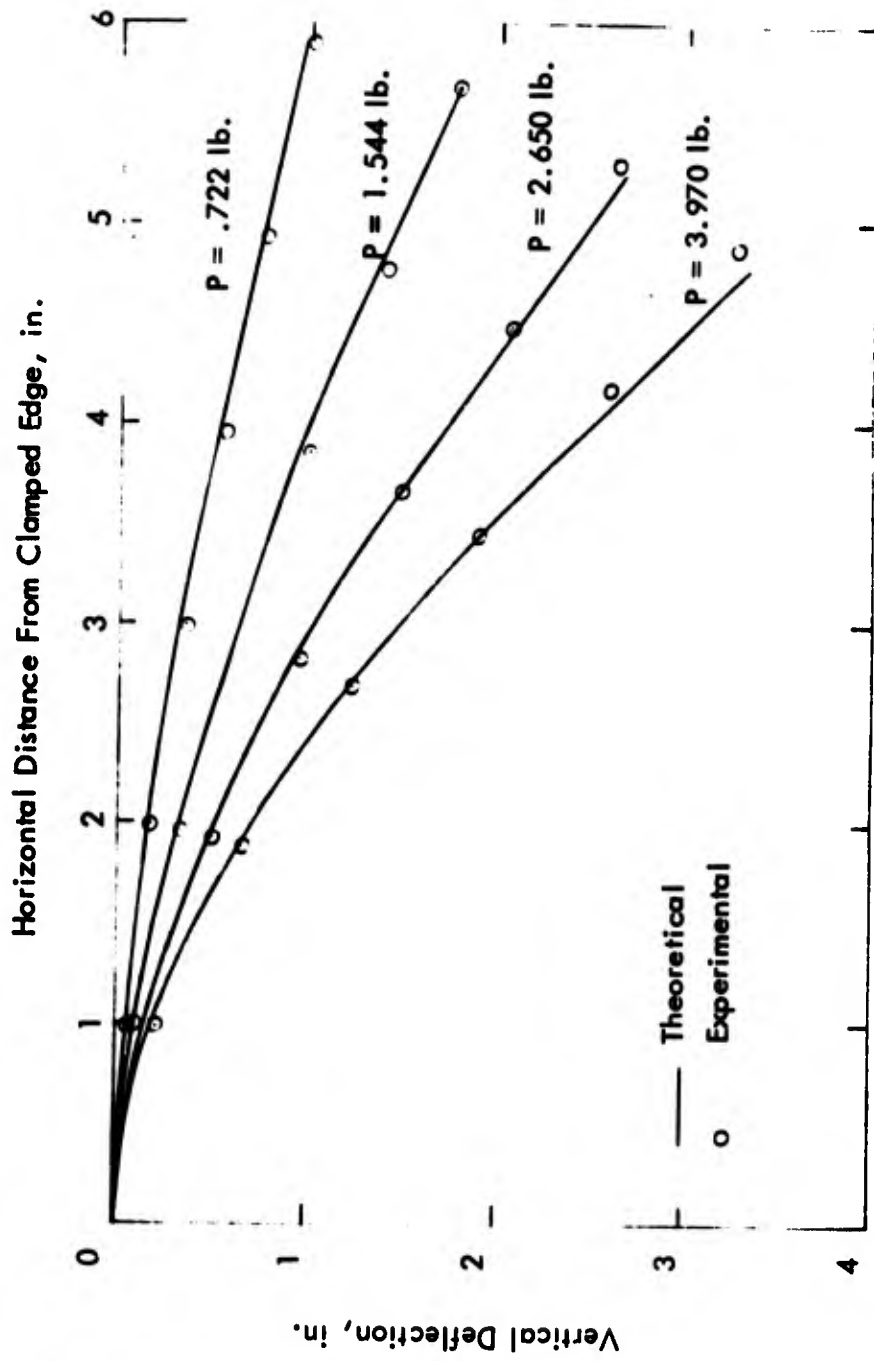


Fig. 3. Deflection Curve of the Leading Edge at Different Loads

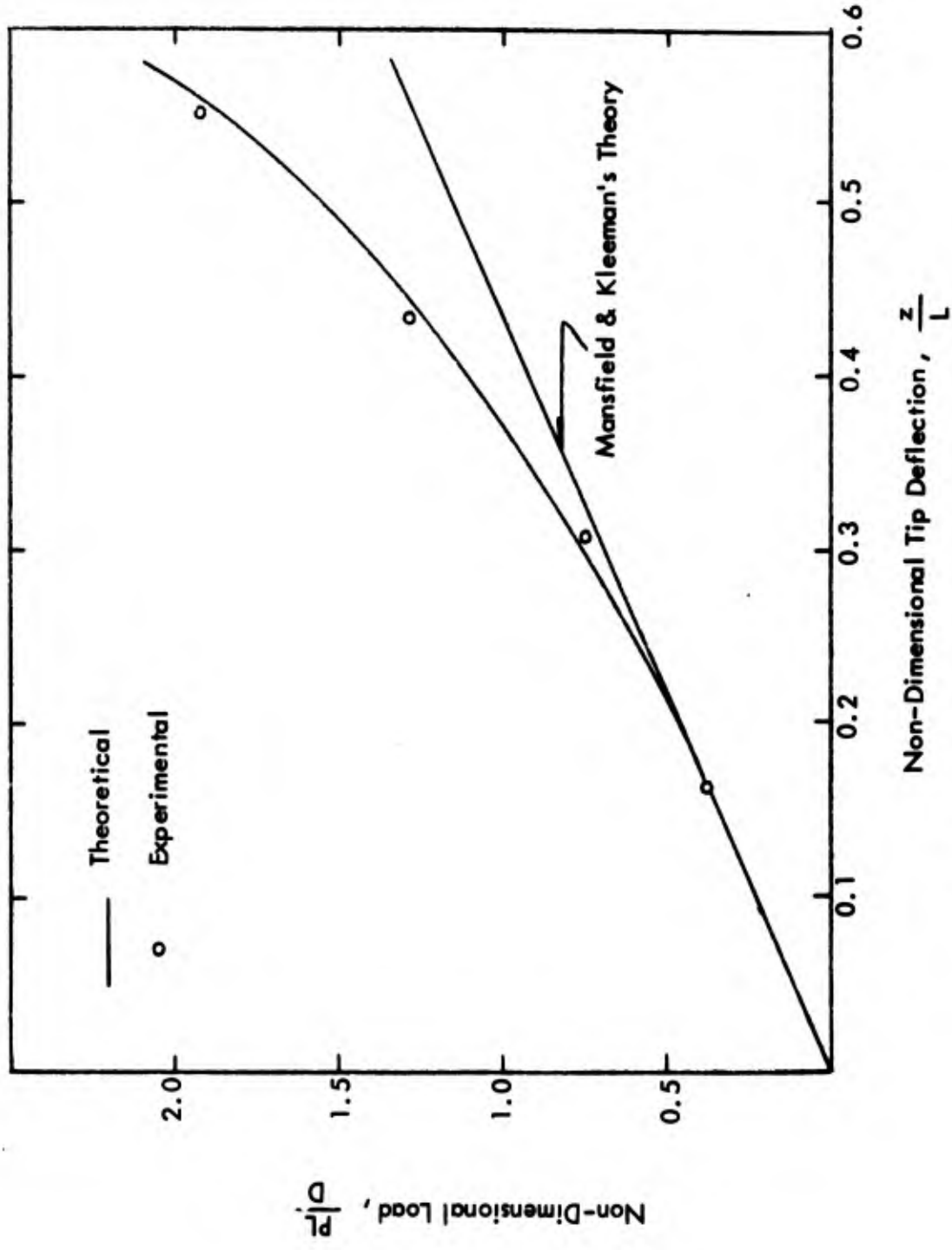


Fig. 4. Tip Deflection Vs. Applied Load

was .0194 inches. Three inches of each specimen were rigidly clamped between heavy ground-steel blocks on the support fixture which resulted in a six inch by six inch square configuration for the actual deforming section.

The steel blocks (for clamping the specimen) were rigidly mounted on a steel angle plate which, in turn, was set level upon a surface plate. Level tolerances were kept to \pm .0002 inches. A grid of node points (1 inch by 1 inch) was painted on the upper surface of each specimen.

The vertical deflections were determined using a vernier height gage (Starrett Model No. 254) using a needle-point dial indicator. An optical-shadow technique was used to determine the point of contact of the dial gage with the plate node-point. To insure true height measurements, a back-up dial indicator, which could measure 0.0001 inch increments was placed on the surface plate to indicate possible deflections on the plate during the vertical height measurements. As a further check to the back-up dial indicator method, (which could cause an error due to its physical contact with the plate specimen), an optical method for measuring the vertical deflections was used which eliminated the use of the dial indicator. A telescope (Bushnell Scope Chief with 6 X magnification), fitted with special lenses for short range viewing, was mounted on the vernier height gage. The scope was precision-levelled with respect to the surface plate. Height readings were measured at the grid node-points from the vernier gage.

The loads at the corner of the plate were applied by suspending weights through a small, free-floating steel eyelet fitted into a small hole drilled

very close to the specimen corner. Load levels were selected so as to permit appreciable non-linear deformation within the proportional limit of the specimen. For the flat plate configuration considered herein, a suitable maximum deflection which exhibits appreciable non-linearity within the proportional limit is a value of $\frac{z}{L} = 0.70$.

Typical experimental results are provided in Figure 3 for the deflection of the edge of the square plate where the load is applied (leading edge) as a function of its length at several levels of applied loads. In Figure 4, the experimental data is given in a non-dimensional form for the deflection of the plate along the edge where the corner load is applied (leading edge). Although similar plots could be made for other deflection locations, the results of Figure 4 are representative and should suffice to determine the validity of the theoretical techniques provided herein.

VII CONCLUSION

The measured deflections of the leading edge at different loads and the measured tip deflections versus load are plotted in Figures 3 and 4. It is seen that the agreement between the experimental values and the deflections calculated by the proposed method is excellent.

The calculation of large bending deflections of thin plates by using Von Karman's non-linear equations is a formidable task even with the aid of computers. The inextensional theory for large deflections by Mansfield and Kleeman has simplified greatly the calculations of deflections of inextensible thin plates. For the plates calculated, Mansfield and Kleeman's theory predicts well the deflections many times the thickness and within about 20% of the length; but when the deflection exceeds this amount, the discrepancy between

Mansfield and Kleeman's theory and experiments increases rapidly with load (Figure 4). The present method gives deflections which check with experiment within a few percent for a tip deflection of more than half of the plate length.

The method shown is an approximate numerical method for calculating large inextensional deflections of cantilever and thin plates. Refinement may be made by considering both $\Delta\bar{y}$ and $\Delta\bar{z}$. $\Delta\bar{y}$ may be calculated by the same principle of virtual work with the unit fictitious load applied along the rearward directions.

Part B

Effect of Bi-Axial Stresses On Low Cycle Fatigue

I SUMMARY AND INTRODUCTION

In recent years, demands for lighter weight structures, together with extensive developments and advances in the knowledge of plasticity theory have encouraged engineers and designers to consider a finite life approach to certain engineering problems. There are many applications of this approach; consider for example the design and fabrication of pressure vessels, landing gears, working parts of guns, missiles, etc., where the total life may involve only some hundreds of thousands of stress cycles. For a limited number of cycles, the material can withstand stresses appreciably above its normal high cycle fatigue limit. The technology of low cycle plastic straining of metals has been applied to the design and successful fabrication of energy absorption devices⁵. The specific energy absorption (SEA) capability of metals under cyclic plastic straining has been found to be high. Hence, the technology of low cycle fatigue is not only of academic interest, but also is useful for many practical structures. It is known that high hydrostatic pressures greatly increase the ductility of metals. On this basis, it appears that certain favorable combined stress states which produce compressive mean stress will increase the low cycle fatigue life of metals. The present report describes the results of a study on low cycle fatigue which includes the effect of steady axial stress on torsional fatigue strength of metals.

II EXPERIMENTAL TEST SET-UP OF LOW CYCLE TORSION TESTER

The apparatus used in this study is described schematically in Figure 5. Photographs of the assembly (See Figures 6, 7, 8 and 9) illustrate the mechanical-electrical layout of the system. The apparatus is designed to apply cyclic torsion strains of known amplitude and frequency to "dumbbell" shaped samples while the samples are under a steady tension or compression load.

The total strain range is set by the adjustment of an eccentric cam mechanism^{(8)*} coupled to a gear rack which oscillates a pinion gear. The amplitude of this oscillation determines the total angular displacement applied to the "driven" end of the sample⁽¹⁰⁾. The cyclic rate is varied with respect to the motor drive rate by means of various sheave⁽⁵⁾ combinations between one of two motors^(3-3A), a 60:1 speed reducer⁽⁷⁾, the magnetic clutch⁽²⁾, shaft, and the camshaft⁽⁸⁾.

The actual number of cycles from initial start to shutdown is predetermined by a preset subtraction counter⁽⁶⁾. This counter also measures the total complete cycles for each run**. The magnetic clutch control unit⁽²⁾ connects the camshaft⁽⁸⁾ to the motor and the engagement is adjusted to control the acceleration forces.

The magnetic clutch⁽²⁾ is engaged after the flywheel⁽⁴⁾ reaches full shaft speed. When the counter⁽⁶⁾ reaches zero, the clutch⁽²⁾ is

*Numbers refer to the designated component in Figure 5.

**A certain overrun results from inertia in the system at high cyclic rates

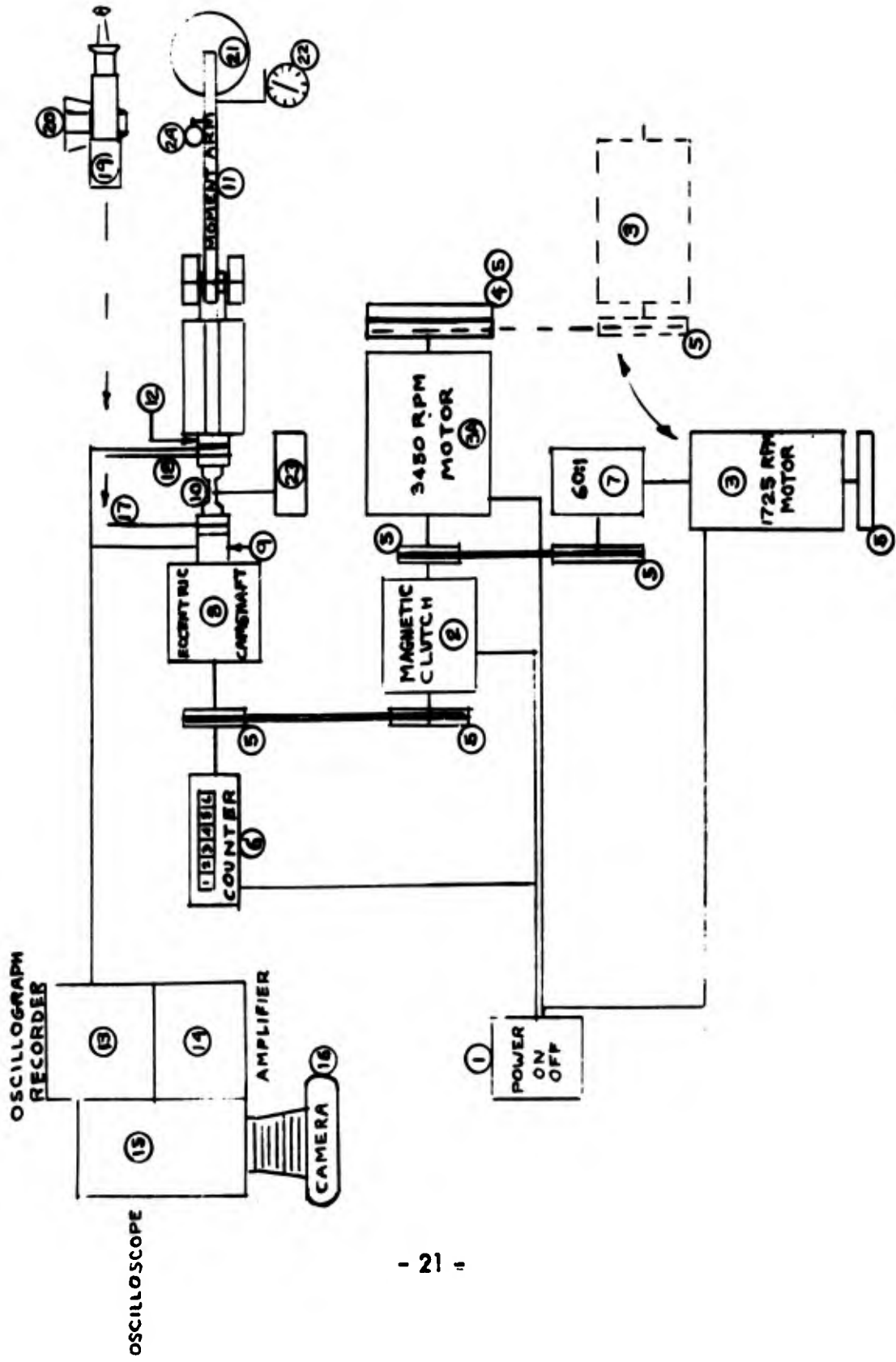


Fig. 5 . Schematic of Bi-Axial Cyclic Torsion Test Apparatus

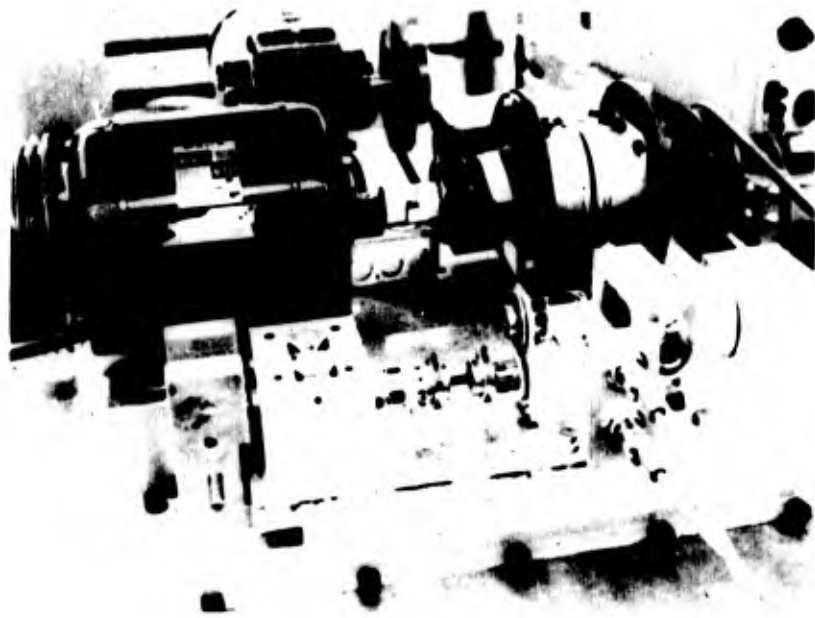


Fig. 6 Close-Up View of Cyclic Torsion Apparatus

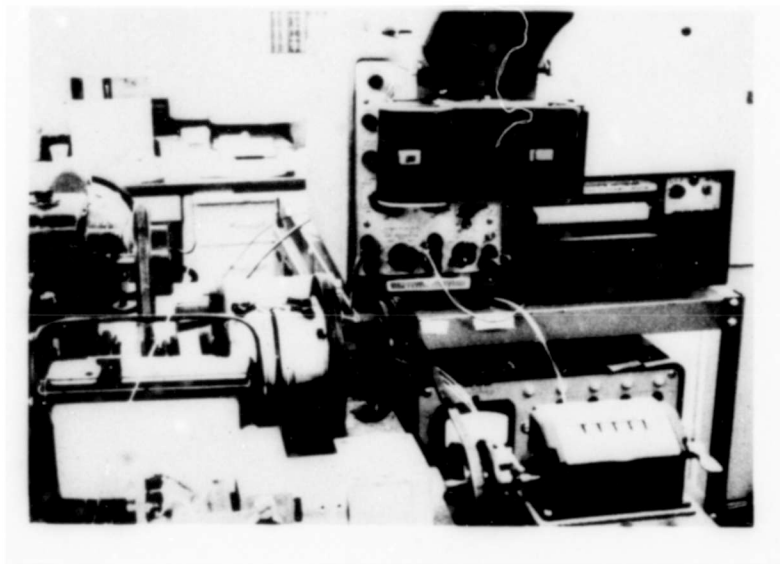


Fig. 7 Close-Up View of Recording Equipment
For Cyclic Torsion Apparatus

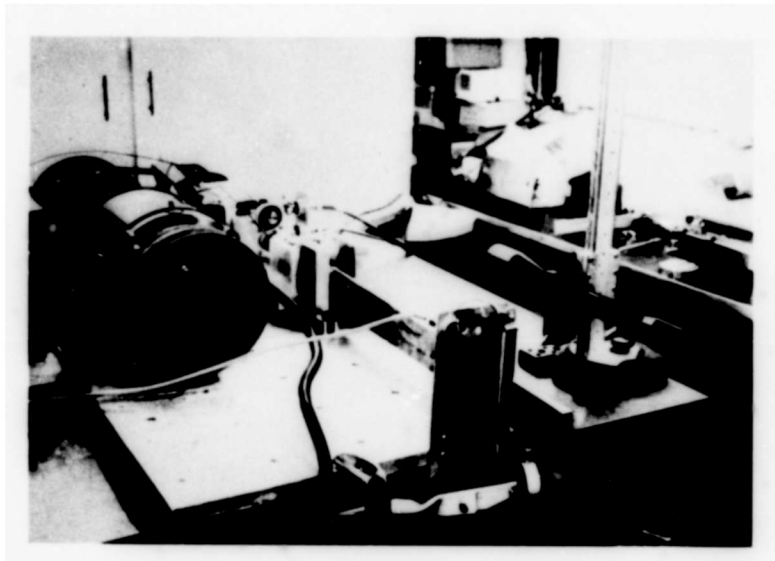


Fig. 8 View of Axial Tension-Compression Beam and
Deflection Recording Technique
For Cyclic Torsion Apparatus

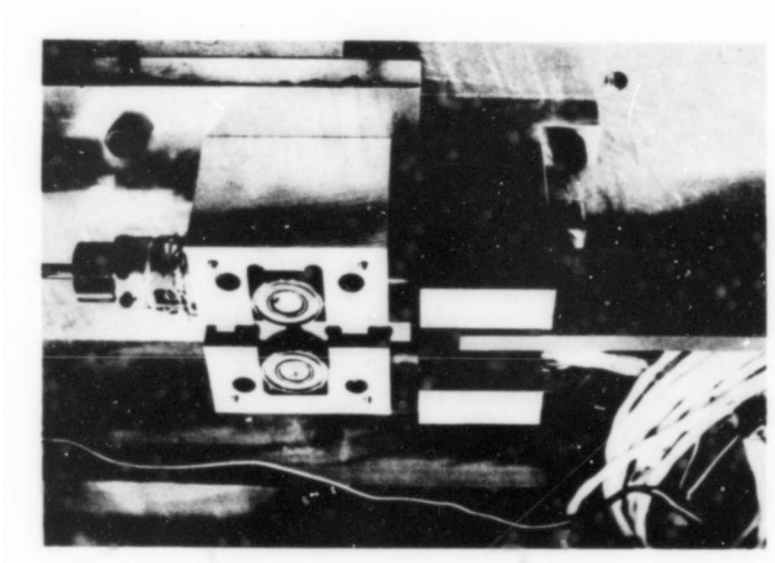


Fig. 9 Close-Up View of Axial Load Bearing Housing
For Cyclic Torsion Apparatus

automatically disengaged. The drive motor⁽³⁾ is then shut off and allowed to coast to a stop without transmitting further motion to the camshaft⁽⁸⁾.

A multi-channel oscillograph recorder⁽¹³⁾ and amplifier⁽¹⁴⁾ control unit were used to record the stress-strain history, as well as the total number of cycles per run. This record provided a time base for the reduction of the recorded data.

The stress history of each cycle is generated by a strain gage⁽¹²⁾ which measures the torque of each cycle. This strain gage⁽¹²⁾ is at the "fixed" end of the sample and is so mounted to be mechanically unaffected by axial loading.

A pulse generating potentiometer⁽⁹⁾ driven by anti-backlash gearing mounted on the eccentric camshaft⁽⁸⁾ provides a record of the angular twist.

Along with the oscillograph recorder⁽¹³⁾, an oscilloscope⁽¹⁵⁾ with a polaroid-land camera attachment⁽¹⁶⁾ was employed to photograph the actual stress-strain hysteresis loop. This provided an accurate method of cross-checking the recorded data, as well as eliminating the need for exhaustive data reduction to determine the stress-strain hysteresis loop shape accurately.

Temperature changes occurring during the test were recorded both visually on an electric thermometer⁽²³⁾ (by the operator), and automatically on a channel of the oscillograph recorder⁽¹³⁾ by means of a thermocouple wire to the galvanometer.

Axial loading was provided through a 20:1 ratio moment arm⁽¹¹⁾ connected directly to the fixed end of the sample bypassing the strain gage. Weights⁽²¹⁾ were suspended from the moment arm to provide loads up to 20,000 psi to the sample. Axial deflection was monitored visually by the operator reading a 1/10,000" dial indicator⁽²²⁾ so that actual growth of the sample could be accurately calculated. In order that this information could be recorded (graphically), a rectilinear potentiometer⁽²⁴⁾ was also attached to the moment arm⁽¹¹⁾.

A. Calibration

Calibration of the pulse generating potentiometer⁽⁹⁾ relative to the recorder and oscilloscope was done optically. A high-powered telescope⁽¹⁹⁾ and a vernier height gage⁽²⁰⁾ were employed along with a deflection pointer⁽¹⁷⁾ mounted on the output end of the camshaft at the sample collet. By accurately measuring the pointer travel, the angular deflection (strain) could be preset or measured within $\pm .01$ degree. Calibration data was obtained for 1%, 2%, 4%, and 7% strain rates.

The strain gage⁽¹²⁾ was calibrated by using a moment arm⁽¹⁸⁾ rigidly mounted to the "fixed" end of the sample. An electronic calibrator and dead-weight loads (to the sample) were applied to achieve calibration of the oscilloscope⁽¹⁵⁾ and oscillograph⁽¹³⁾ records.

The oscilloscope recorder thermocouple, as well as the electric thermometer⁽²³⁾ were both calibrated simultaneously against a 1% tolerance mercury thermometer in a controlled (temperature) rise bath.

The calibration of the rectilinear potentiometer⁽²⁴⁾ and oscillograph record were accomplished against the dial indicator.

III TEST SPECIMENS

Two types of metallic materials were used for the cyclic torsion fatigue test and discussion; they were aluminum alloy 2024 (T4 and T351) and Beryllium Copper 25. Their mechanical properties are given in Table I. Fatigue tests were conducted using the thin wall tubular structure shown in Figure 10. The rigidity of the supporting ends is much stronger than the central portion of the test tube; thus, the recorded twist is produced mainly by the reduced gage portion of the tube.

TABLE I
Mechanical Properties of Test Specimens

Material		Yield Strength psi	Ultimate Strength psi	Modulus of Rigidity, G_{psi}	Density lb/in ³	Elongation In 2 Inches, %
Beryllium Copper		75,000	115,000	7.0×10^6	0.297	5
Aluminum Alloy 2024	T4	47,000	68,000	3.97×10^6	0.100	19
	T351	40,000	60,000	3.97×10^6	0.100	10

IV TEST RESULTS

A number of specimens of aluminum alloy 2024 and beryllium copper were tested under different amounts of cyclic torsional strain subject to different

627 24

Fixed End

Driving End

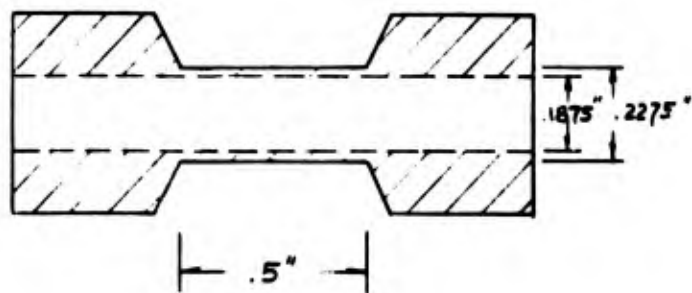


Fig. 10 Typical Specimen Dimensions

axial stresses at 102 cycles/min. The test results are tabulated in Table II. The specimens are subject to a given twist per unit length. The outermost torsional strain varies linearly with the outside diameter of the specimen. Since this diameter varies by a small amount from one specimen to another, the outermost torsional strain varies with the diameter. It is seen from Table II that these specimens having a larger outside diameter are subject to larger alternate torsional strain which results in a lower number of cycles to failure.

A. Aluminum Alloy

A plot of the number of cycles to failure as a function of plastic torsional strain for aluminum alloy 2024-T4 is given in Figure 11. The effect of axial stress on the cycles to failure for aluminum alloy 2024 T-351 is shown in Figure 12 for 3% total shear strain and in Figure 13 for 4% total shear strain. The effect of axial stress on the total energy dissipated for aluminum alloy 2024 T-351 is shown in Figure 14 for 3% total shear strain and in Figure 15 for 4% total shear strain.

B. Beryllium Copper

Similar to the plots shown for the aluminum alloys, a plot of the number of cycles to failure with plastic torsional strain is given in Figure 16 for beryllium copper. Effects of axial stress on the cycles to failure are shown in Figure 17 for 3% total shear strain and in Figure 18 for 4.5% total shear strain. Finally, the total energy dissipated by the beryllium copper during cyclic torsion as affected by axial stress is shown in Figure 19 for 3% total shear strain and in Figure 20 for 4.5% total shear strain.

TABLE II

Cyclic Torsion Tests for Al 2024 T4

Total Shear Strain Range $\Delta\epsilon_T, \%$	Plastic Shear Strain Range $\Delta\epsilon_p, \%$	Axial Stress psi	Maximum Shear Stress τ_{max}, psi	Total Energy Dissipated 10^6 in-lb/lb	Number of Cycles to Failure N
2.04	.375	0	33,100	2.68	1,855
2.04	.387	0	32,900	2.02	1,636
2.04	.423	0	32,100	3.50	2,027
2.04	.392	0	32,700	2.18	1,297
2.04	.409	0	32,400	1.79	1,025
2.04	.376	0	33,000	1.69	1,280
3.06	1.23	0	36,300	1.73	324
3.05	1.22	0	36,200	1.51	293
3.06	1.30	0	35,000	1.45	273
3.06	1.26	0	35,600	2.05	401
3.01	1.29	0	34,200	.903	227
3.01	1.30	0	33,900	1.25	316
3.02	1.33	0	33,400	.795	197
3.04	1.53	+ 10,000	30,000	.792	219
3.03	1.58	+ 10,000	30,200	1.38	399

3.08	1.26	0	35,800	2.05	401
3.01	1.29	0	34,200	.903	227
3.01	1.30	0	33,900	1.25	316
3.02	1.33	0	33,400	.795	197
3.04	1.53	+ 10,000	30,000	.792	219
3.03	1.58	+ 10,000	30,200	1.38	399
3.04	1.40	+ 10,000	32,500	.889	300
3.03	1.40	+ 10,000	32,300	.386	129
3.03	1.38	- 10,000	32,900	1.29	359
3.04	1.30	- 10,000	34,500	1.38	414
4.46	2.61	0	36,800	1.80	142
4.48	2.58	0	37,600	1.07	82
4.46	2.58	0	37,400	1.83	147
4.48	2.58	0	37,600	1.17	90
4.45	2.57	0	37,400	1.74	133
6.08	4.07	0	40,000	1.24	52
6.06	4.09	0	39,200	.662	29
6.09	4.08	0	39,800	.947	41
6.09	4.10	0	39,400	1.01	42
6.09	4.06	0	40,200	1.65	69

B

TABLE II (Continued)

Cyclic Torsion Tests for AI 2024 T351

Total Shear Strain Range $\Delta\epsilon_T, \%$	Plastic Shear Strain Range $\Delta\epsilon_p, \%$	Axial Stress psi	Maximum Shear Stress τ_{max}, psi	Total Energy Dissipated 10^6 in-lb/lb	Number of Cycles to Failure N
2.99	2.99	0	35,100	1.56	558
2.99	1.26	0	34,300	1.40	236
2.99	1.19	0	35,700	1.04	176
2.99	1.21	0	35,400	1.69	273
2.99	1.12	0	36,000	1.63	264
2.99	1.25	0	34,600	1.46	244
3.03	1.45	- 10,000	31,500	.876	229
3.03	1.52	- 10,000	30,100	1.07	273
3.03	1.56	- 10,000	29,200	1.14	282
3.03	1.46	- 20,000	31,100	1.59	438
3.03	1.52	- 20,000	30,000	1.29	361
3.03	1.40	- 20,000	32,300	2.05	558
3.03	1.47	- 20,000	30,900	1.81	500
3.03	1.41	- 20,000	32,100	2.28	646
3.03	1.45	- 30,000	31,500	1.90	523
3.03	1.40	- 30,000	32,400	1.98	560

D

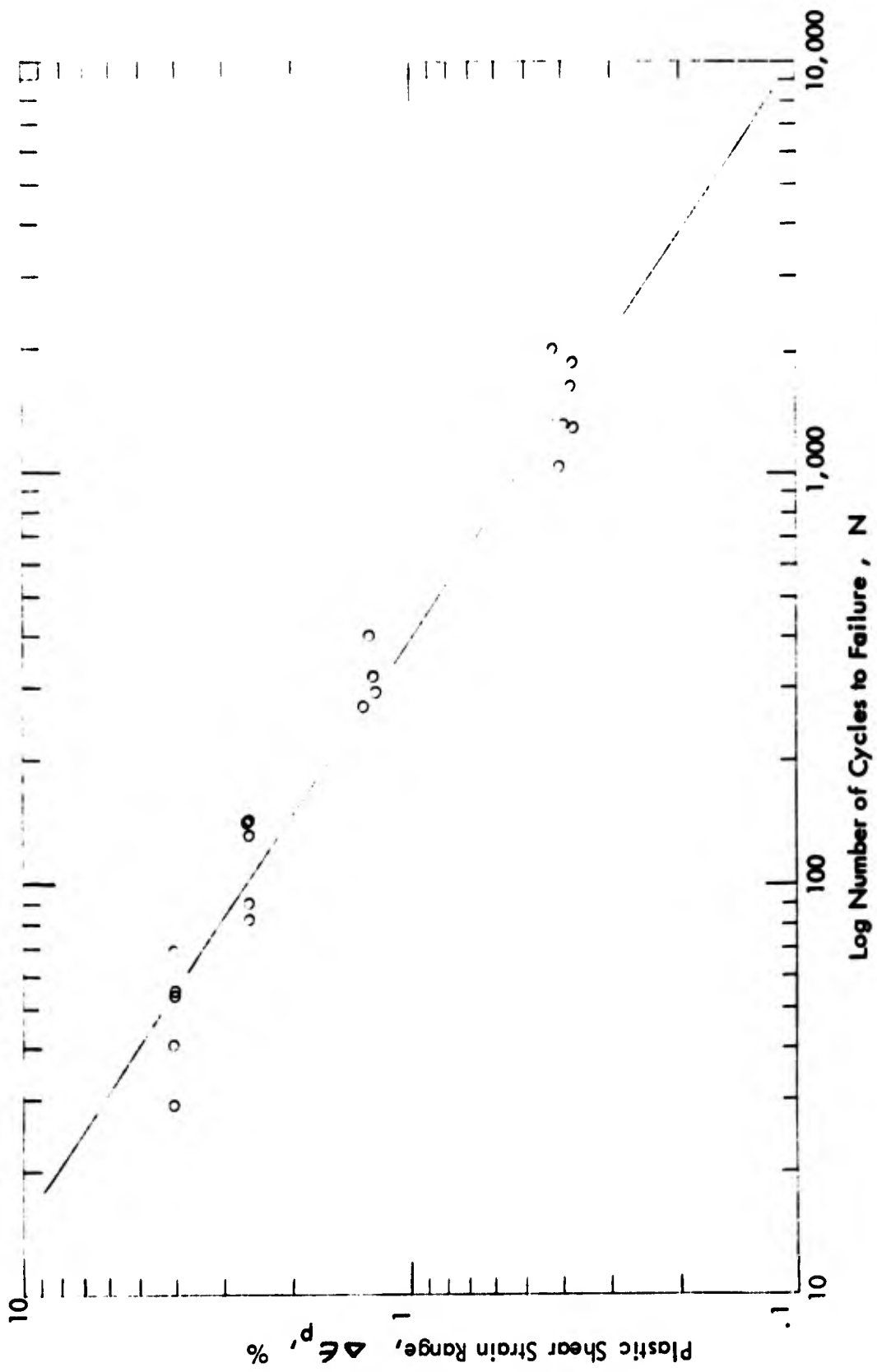
3.03	1.41	- 20,000	32,100	1.81	500
3.03	1.45	- 30,000	31,500	1.90	523
3.03	1.40	- 30,000	32,400	1.98	560
3.98	2.26	0	34,000	2.25	184
3.97	2.21	0	34,900	1.28	145
3.98	2.56	0	28,000	1.08	114
3.97	2.18	0	35,500	.98	111
3.96	2.43	+ 10,000	30,300	.51	64
3.96	2.27	+ 10,000	33,600	.56	72
3.96	2.40	+ 10,000	31,000	.81	103
3.96	2.26	+ 10,000	33,800	.79	101
3.98	2.30	- 10,000	33,400	1.15	140
3.98	2.12	- 10,000	36,800	.44	62
3.98	2.40	- 10,000	31,300	.65	78
3.97	2.28	- 10,000	33,500	1.35	163
3.97	2.27	- 10,000	33,700	2.40	294
3.96	2.25	- 20,000	33,900	1.17	150
3.96	2.30	- 20,000	33,100	2.19	285
3.96	2.52	- 20,000	28,700	1.07	134
3.96	2.20	- 20,000	35,000	1.49	183

TABLE II (Continued)
Cyclic Torsion Tests for Beryllium Copper 25

Total Shear Strain Range $\Delta \epsilon_T, \%$	Plastic Shear Strain Range $\Delta \epsilon_p, \%$	Axial Stress psi	Maximum Shear Stress τ_{max}, psi	Total Energy Dissipated 10^6 in-lb/lb	Number of Cycles to Failure N
2.04	.492	0	54,100	2.512	7,800
3.01	1.40	0	56,600	.359	241
3.01	1.29	0	60,400	.224	173
3.01	1.31	0	59,700	.241	183
3.01	1.30	0	60,000	.336	258
3.01	1.36	0	57,800	.282	197
3.01	1.44	+ 7,400	54,800	.572	426
3.01	1.34	+ 7,300	58,700	.340	375
3.01	1.55	+ 10,000	51,100	.566	717
3.02	1.50	+ 10,000	53,200	.325	261
3.01	1.38	+ 10,000	57,100	.309	367
3.02	1.49	- 10,000	53,700	.548	418
3.02	1.48	- 10,000	54,000	.771	520
3.04	1.33	- 10,000	59,400	.230	227
3.02	1.45	- 10,000	55,000	.537	423
3.02	1.57	- 20,000	50,700	.717	513
3.02	1.64	- 20,000	48,400	.737	523
3.03	1.62	- 20,000	49,400	.497	394
3.03	1.52	- 20,000	52,800	.385	347
3.03	1.54	- 20,000	52,300	1.47	1,277
3.04	1.64	- 30,000	48,900	.453	401
3.04	1.59	- 30,000	50,500	1.39	1,228
3.04	1.57	- 30,000	51,600	1.57	1,509
3.03	1.55	- 30,000	51,800	.582	482

D

3.03	1.54	- 20,000	52,300	1.47	1,277
3.04	1.64	- 30,000	48,900	.453	401
3.04	1.59	- 30,000	50,500	1.39	1,228
3.04	1.57	- 30,000	51,600	1.57	1,509
3.03	1.55	- 30,000	51,800	.582	482
3.03	1.54	- 30,000	52,000	.850	820
3.98	2.30	0	58,800	.760	250
3.97	2.19	0	62,400	.626	228
4.46	2.58	0	65,800	.460	70
4.46	2.53	0	67,400	.713	116
4.46	2.52	0	68,000	.567	100
4.48	2.70	+ 10,000	62,300	.349	55
4.48	2.75	+ 10,000	61,000	.521	81
4.48	2.75	+ 10,000	60,600	.489	80
4.48	2.68	+ 10,000	62,700	.429	72
4.47	2.61	+ 10,000	65,300	.306	49
4.45	2.55	- 5,000	66,600	.926	164
4.45	2.49	- 5,000	68,800	.577	103
4.45	2.57	- 5,000	65,700	.689	122
4.46	2.50	- 5,000	68,500	1.04	209
4.48	2.69	- 10,000	62,900	.556	99
4.48	2.75	- 10,000	60,500	.523	90
4.48	2.69	- 10,000	62,600	.591	115
4.44	2.57	- 10,000	65,500	1.08	179
4.45	2.72	- 10,000	60,800	.980	203
4.45	2.77	- 20,000	59,000	1.36	272
4.45	2.75	- 20,000	50,500	1.71	331
4.45	2.68	- 20,000	61,700	1.83	313



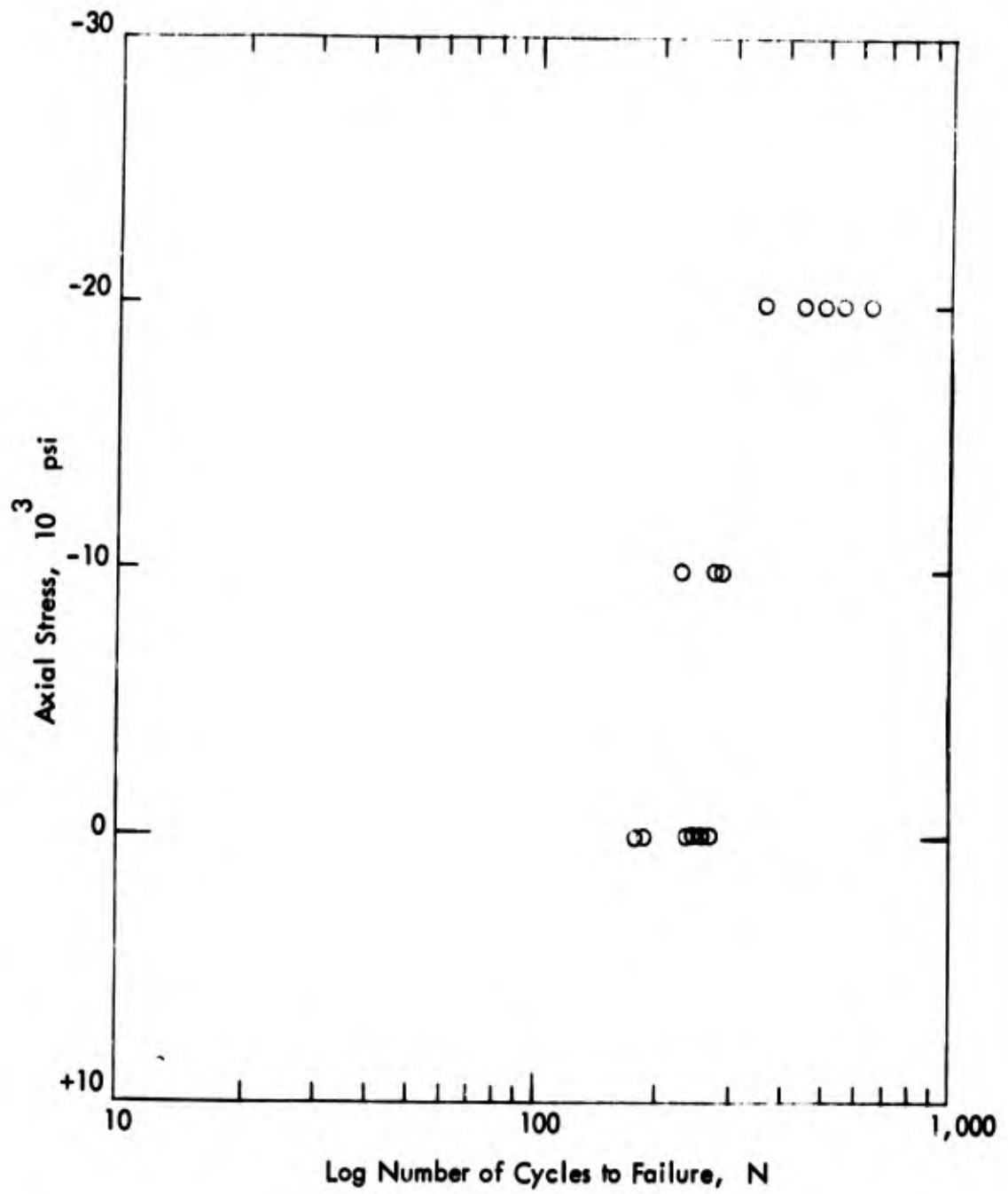


Fig. 12 Effect of Axial Stress on Cyclic Torsion Fatigue Failure of Aluminum Alloy 2024 T351 With 3% Total Shear Strain

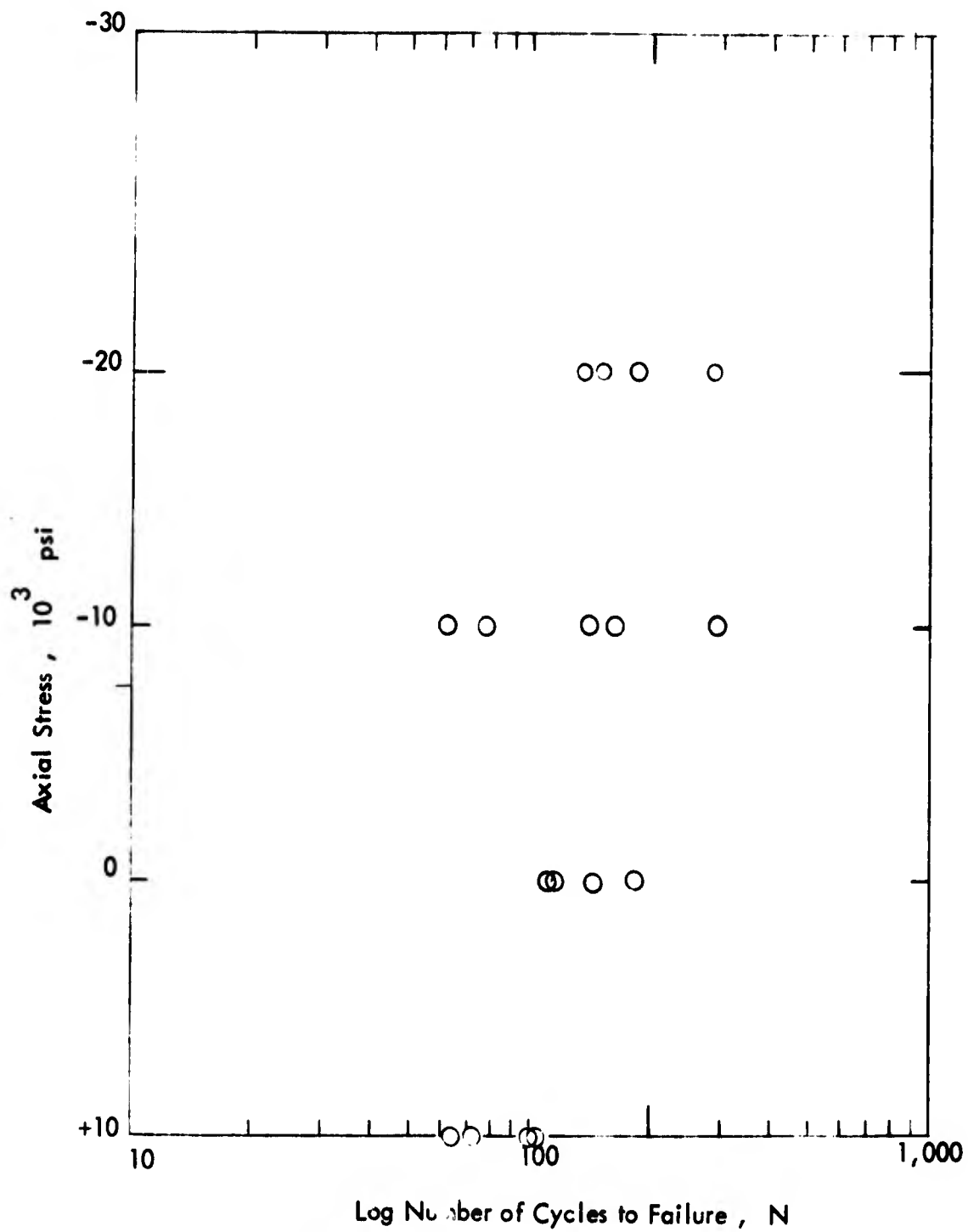


Fig. 13 Effect of Axial Stress on Cyclic Torsion Fatigue Failure of Aluminum Alloy 2024 T351 With 4% Total Shear Strain

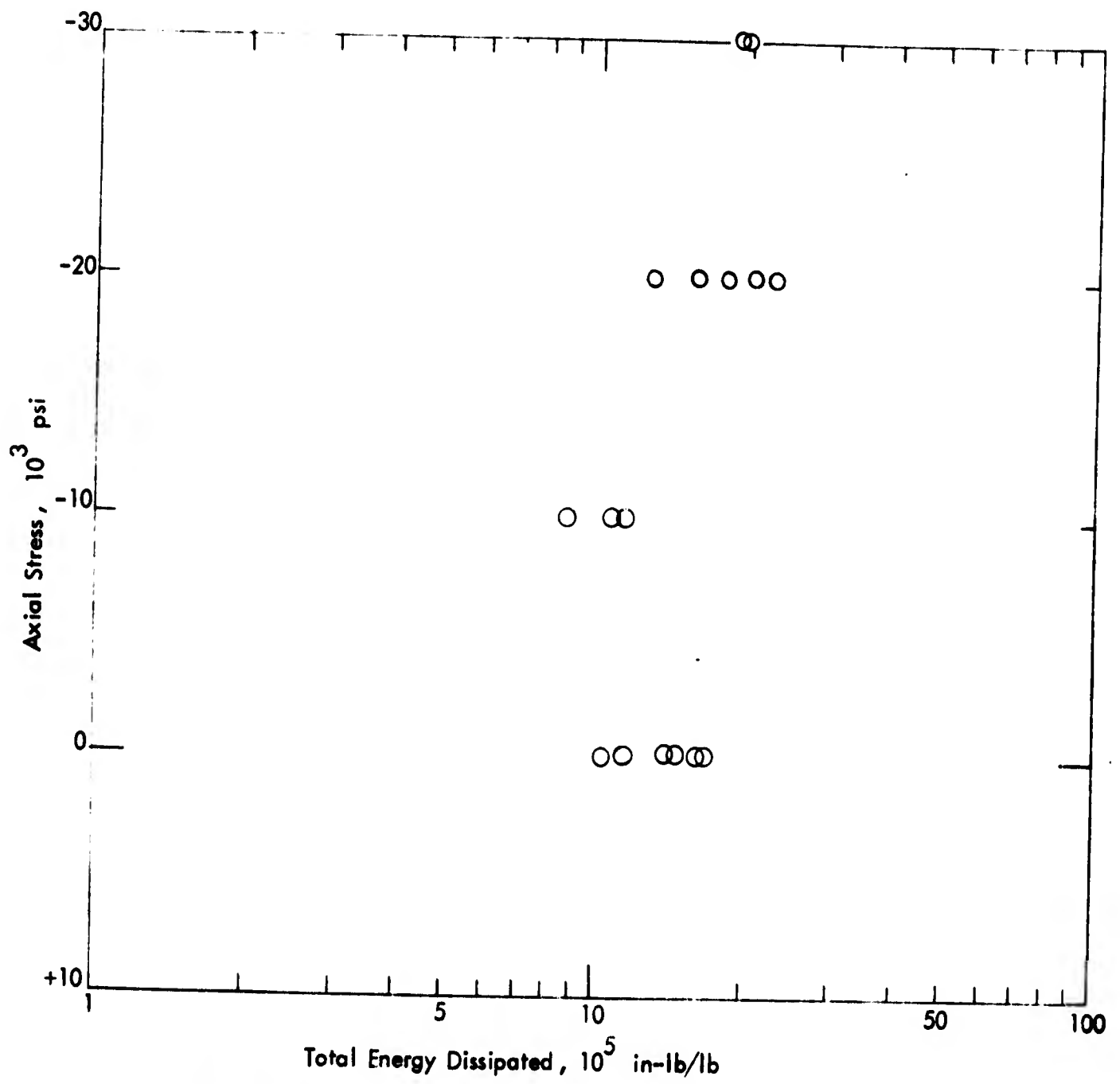


Fig. 14 Variation of Total Energy Dissipated In
Cyclic Torsion at 3% Total Shear Strain With
Axial Load for Aluminum Alloy 2024 T351

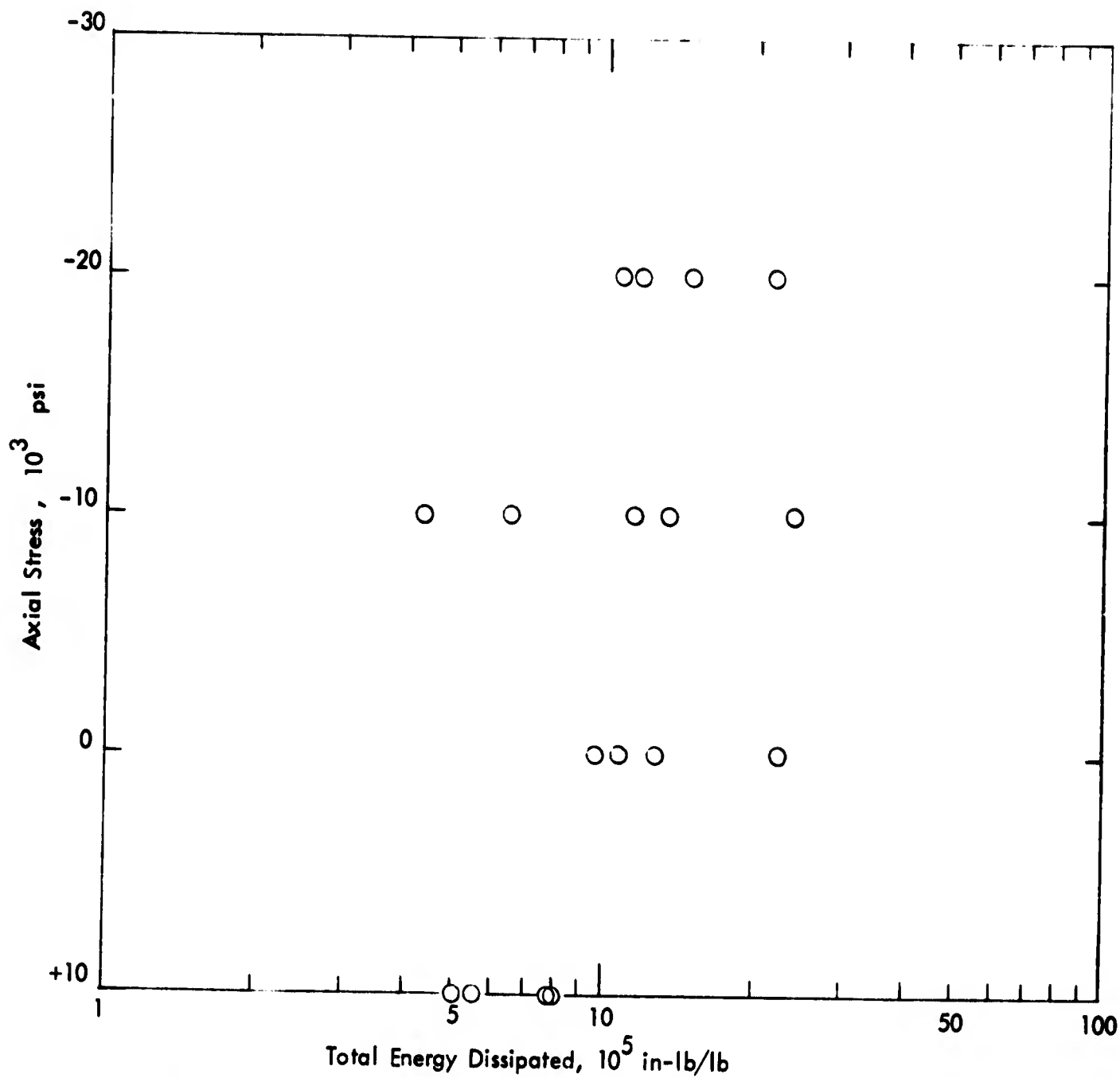


Fig. 15 Variation of Total Energy Dissipated In Cyclic Torsion
at 4% Total Shear Strain With Axial Load
For Aluminum Alloy 2024 T351

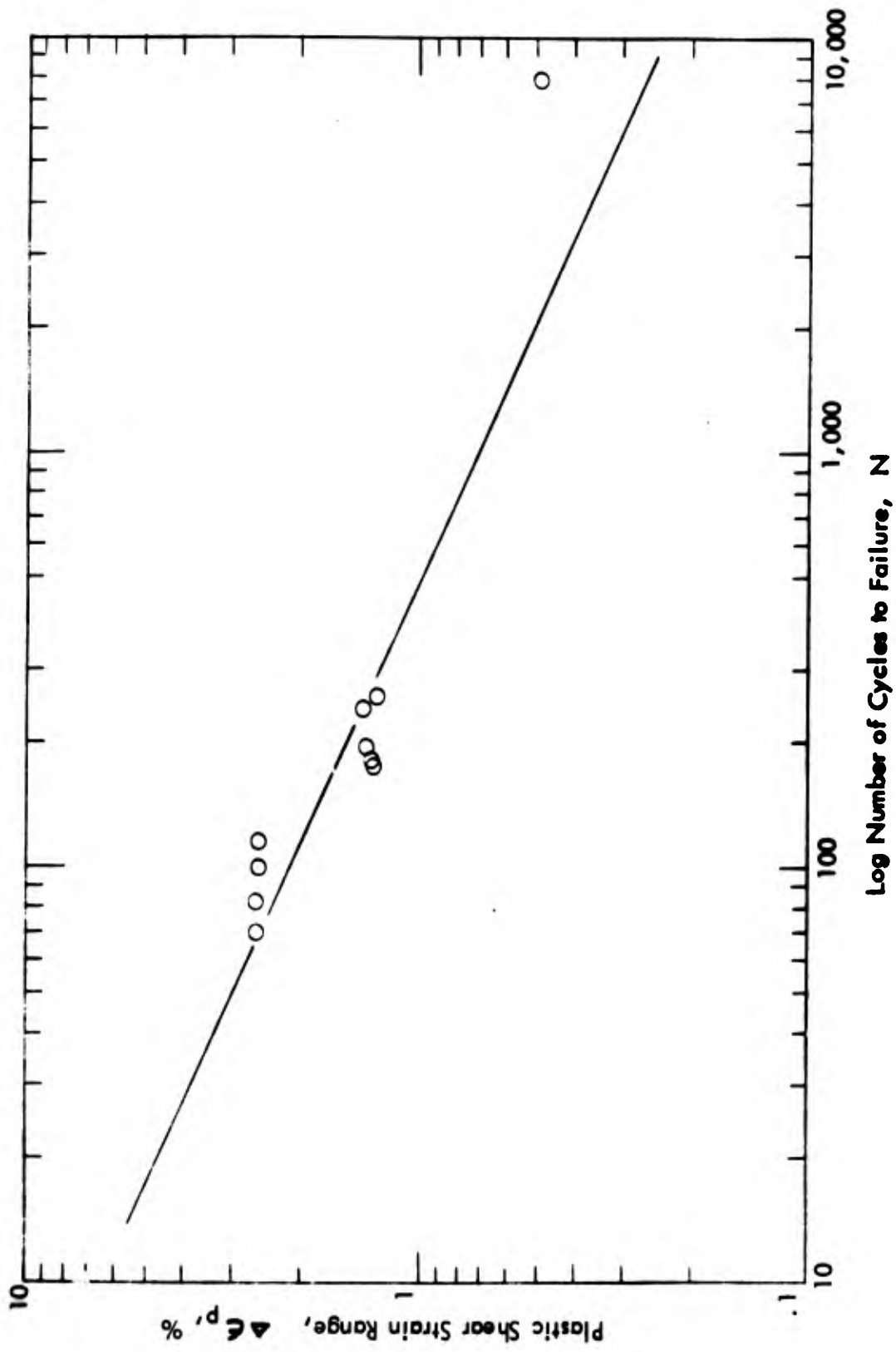


Fig. 16 Cyclic Tension Fatigue Curve for Beryllium Copper

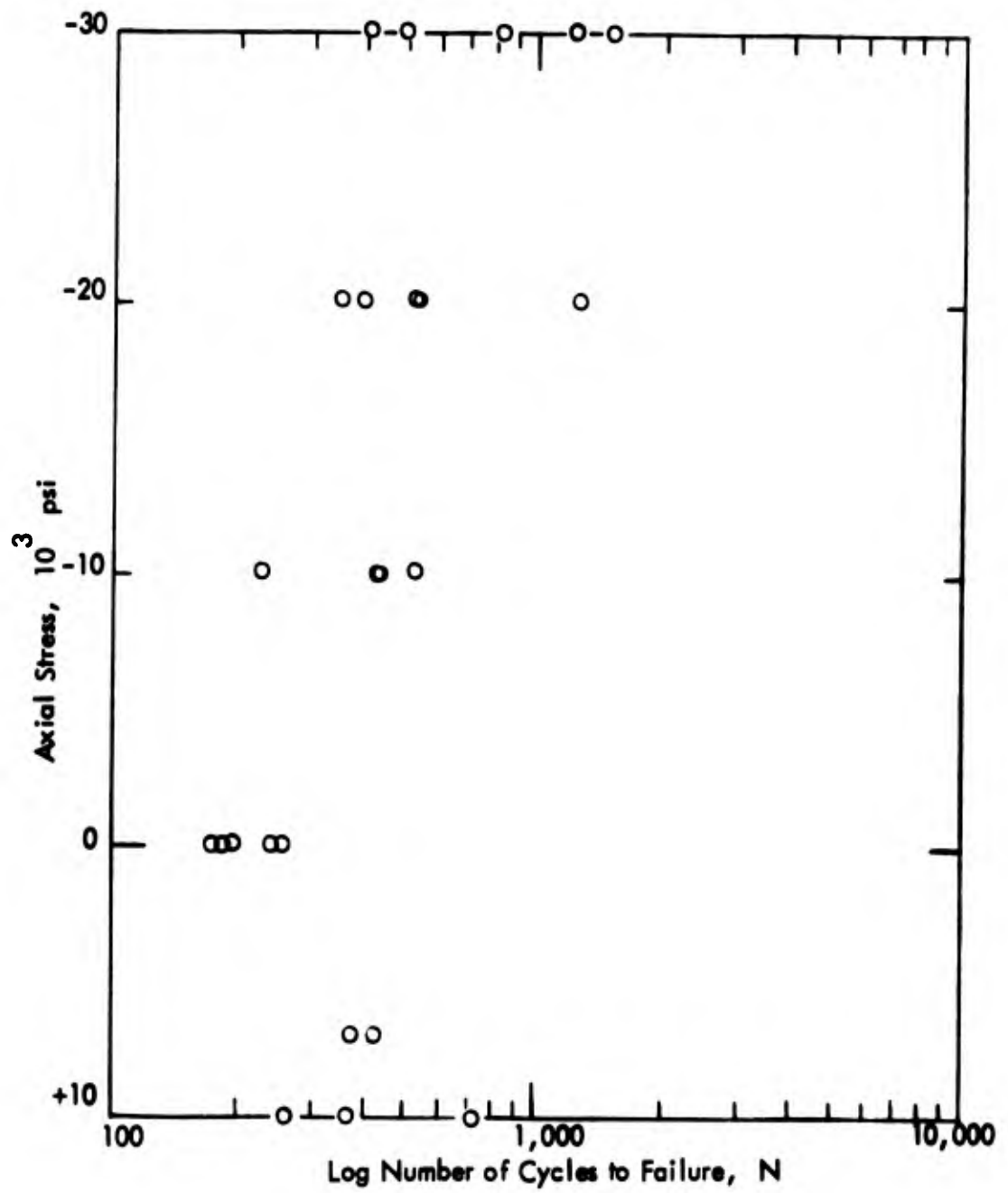


Fig. 17 Effect of Axial Stress on Cyclic Torsion Fatigue Failure of Beryllium Copper With 3% Total Shear Strain

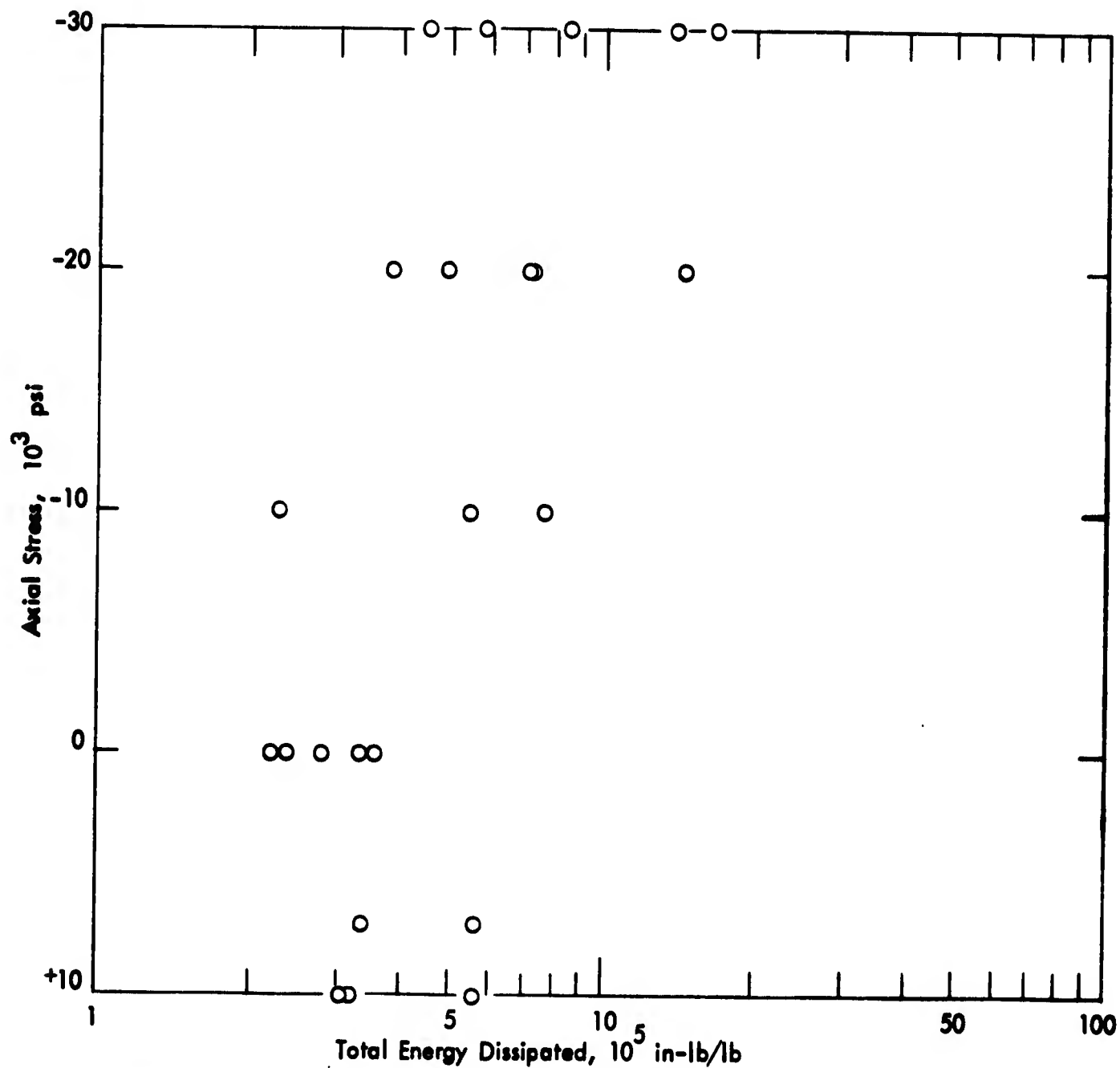


Fig. 19 Variation of Total Energy Dissipated in Cyclic Torsion
at 3% Total Shear Strain With Axial Load
For Beryllium Copper

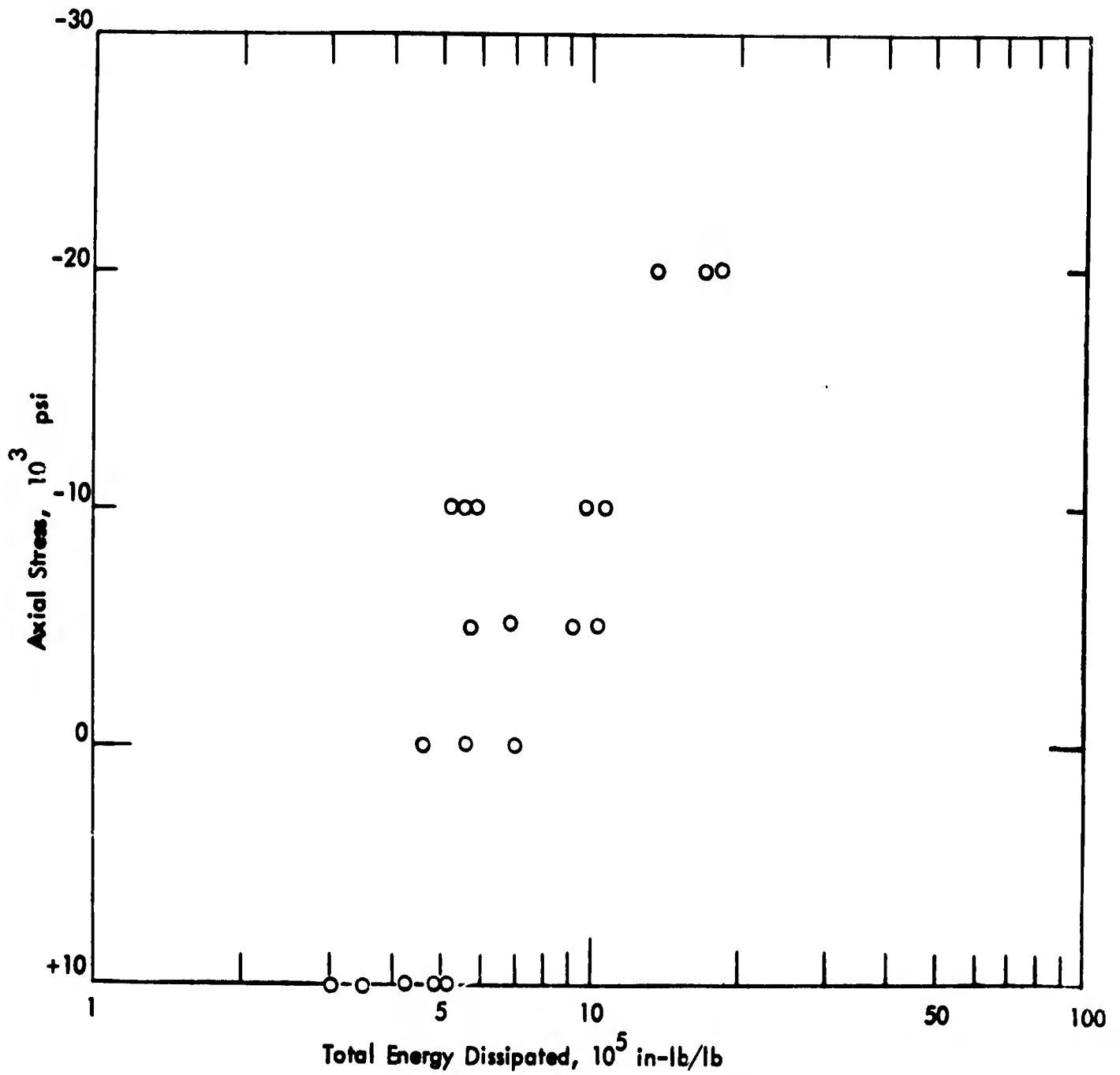


Fig. 20 Variation of Total Energy Dissipated in Cyclic Torsion at 4.5% Total Shear Strain With Axial Load for Beryllium Copper

V DISCUSSION AND CONCLUDING REMARKS

Considerable work has been expended on the study of fatigue under combined loadings; see for example Reference 6. Review of the open literature indicates that there is little low-cycle fatigue data in torsion under constant axial stress. The present tests provide some basic data for this case. In general, fatigue data experiences quite a bit of scatter and as a result, extensive tests are required before conclusive results can be drawn. However, based on the present study, several preliminary conclusions can be made as follows:

A. Correlation of Data with Coffin's Equation

From Figure 11, the variation of $\log \Delta \epsilon_p$ vs $\log N$ is linear where $\Delta \epsilon_p$ is the range of plastic shear strain and N is the number of cycles to fracture. This linear relationship in the log-log plane seems to satisfy the type of equation proposed by Coffin⁷.

$$\begin{aligned} N^m \Delta \epsilon_p &= C \\ m \log N + \log \Delta \epsilon_p &= \log C \end{aligned} \tag{32}$$

where m is the slope of this straight line and C is the value of $\Delta \epsilon_p$ at $N = 1$. If $\Delta \epsilon_p$ is in %, m and C for aluminum alloy 2024 T4 were found to be .7075 and 68.12, respectively. Unfortunately, due to time limitations, an insufficient number of specimens of beryllium copper have been tested. However, based on existing data, if an equation of Coffin's type is assumed to best fit the data points in Figure 16, the corresponding values of m and C were found to be .4771 and 19.20.

B. Effect of Axial Stress on Fatigue and Absorbed Energy

Based on the data shown in Figure 18 and 20 when the beryllium copper specimens are subjected to an alternate torsional strain of $\pm 4.5\%$, the presence of steady tensile stress clearly decreases the number of alternate torsional cycles to fatigue failure and the total energy absorbed in fatigue life. On the other hand, steady axial compressive stress increases the number of cycles to failure and the total absorbed energy. When the same material is subjected to an alternate torsional strain of $\pm 3\%$, (as shown in Figures 17 and 19), a steady tensile stress did not decrease the number of cycles to failure or the total absorbed energy; however, a steady axial compressive stress did considerably increase the number of cycles to failure and the absorbed energy. For the aluminum alloy specimens, the data shown in Figures 12, 13, 14, and 15 are quite scattered. A general trend does exist in that a steady compressive stress increases the number of cycles to failure and the total energy absorbed.

C. Effects Due to Work Hardening

When a metal is twisted to a strain "e" beyond its elastic limit, the stress-strain curve is a straight line up to the elastic limit and then decreases in slope. If this metal is then unloaded, the first portion of unloading is again a straight line. The transition from elastic unloading to plastic deformation during reverse loading takes place at a reversed stress much lower than the elastic limit of the initial loading. This phenomenon is known as the Bauschinger effect. The presence of the Bauschinger effect in polycrystalline metal can be explained by considering two neighboring crystals which undergo

the same (tensile) strain, but which have different stress-strain relations as caused by the difference in orientations⁸. On unloading, both are assumed to behave elastically. When the applied load is zero, one will be in tension, and the other in compression. On unloading in the opposite sense, the residual stress in the softer grain is in the direction to make it yield even earlier than before. The combination is softer for the reverse loading than it was in the virgin state. This explains the Bauschinger effect which is the main cause of the hysteresis loop. Rigorous calculation of the hysteresis loop of a polycrystalline aggregate was shown by Lin and Ito in 1964⁹.

In the present tests, under constant alternate torsional strain, cyclic stress increases rapidly in the first five to ten cycles for aluminum alloy 2024 with or without axial load. Thereafter, the cyclic stress remains approximately constant until fracture occurs (See Figures 21, 22 and 23). Hence, aluminum alloy 2024 work hardens in the early stage of fatigue loading. On the other hand, the beryllium copper specimens, either with or without axial load initially experience the greatest maximum shear stress, and then for succeeding cycles, the maximum shear stress decreased monotonically as shown in Figures 24, 25 and 26. Thus, beryllium copper work softens with fatigue loading with or without axial stress.

Under axial compressive load, the plastic axial strain increases with cycles of torsional loading for both aluminum alloy and beryllium copper (See Figures 22, 23, 25 and 26). This agrees qualitatively with the kinematic hardening theory proposed by Prager¹⁰; i. e., the loading surface moves in

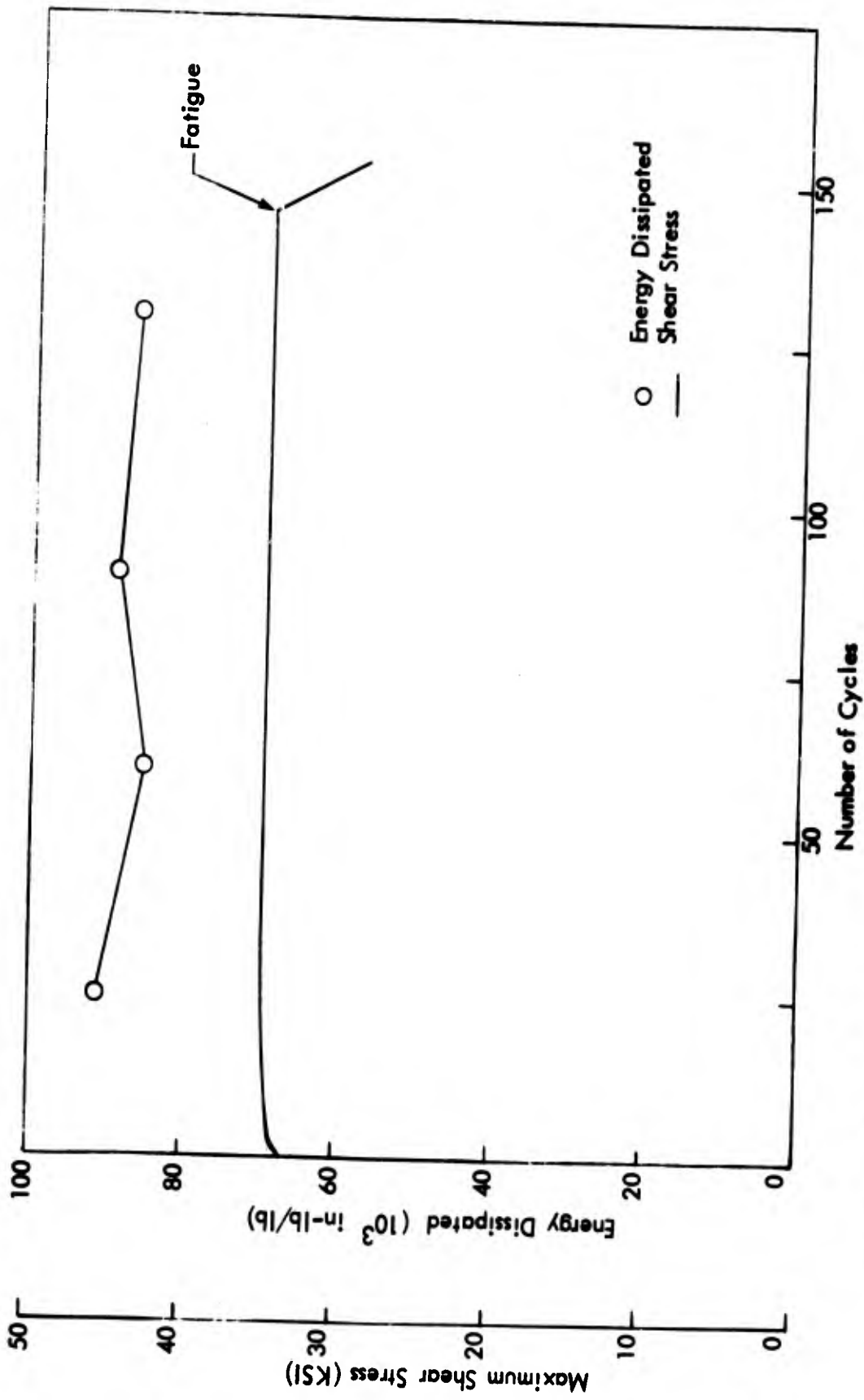


Fig. 21 Typical Changes of Maximum Shear Stress and Energy Dissipated Due to Cyclic Torsion For Aluminum Alloy 2024 T351 at 4% Total Shear Strain

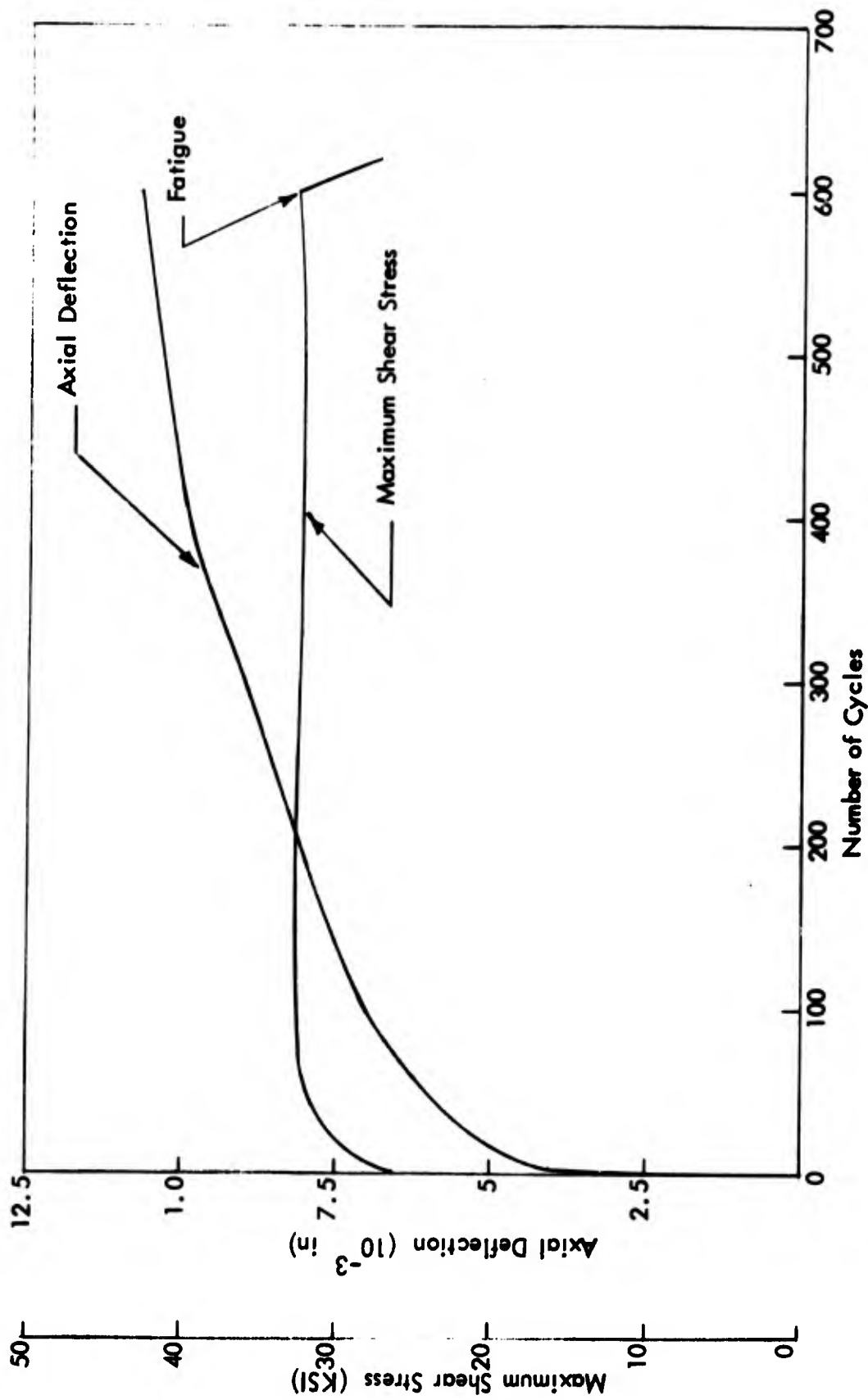


Fig. 22 Typical Changes of Maximum Shear Stress and Axial Deflection
 Due to Cyclic Torsion for Aluminum Alloy 2024 T351
 at 3% Total Shear Strain and 20,000 psi Axial Compression

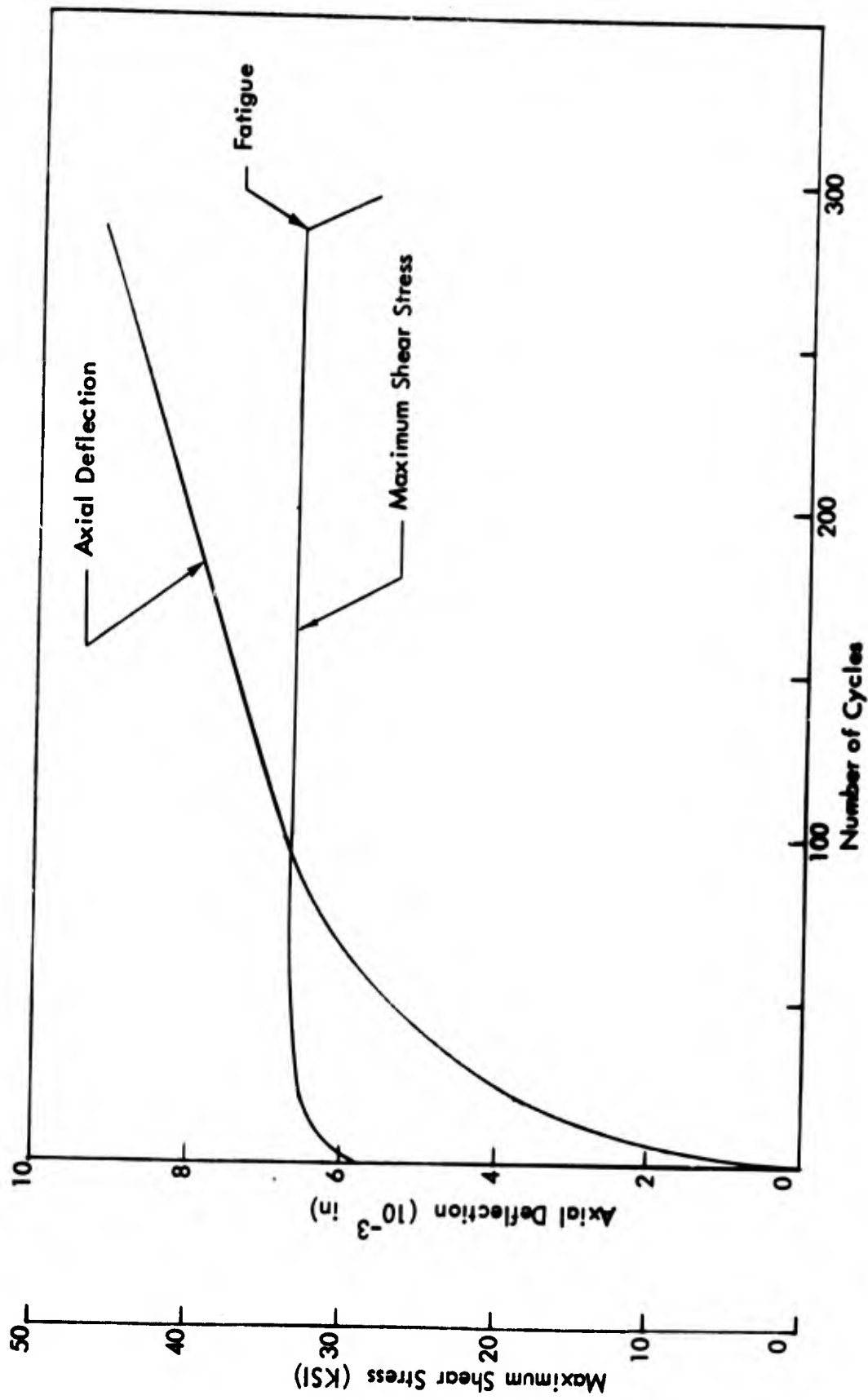


Fig. 23 Typical Changes of Maximum Shear Stress and Axial Deflection Due to Cyclic Torsion for Aluminum Alloy 2024 T351 at 4% Total Shear Strain and 20,000 psi Axial Compression

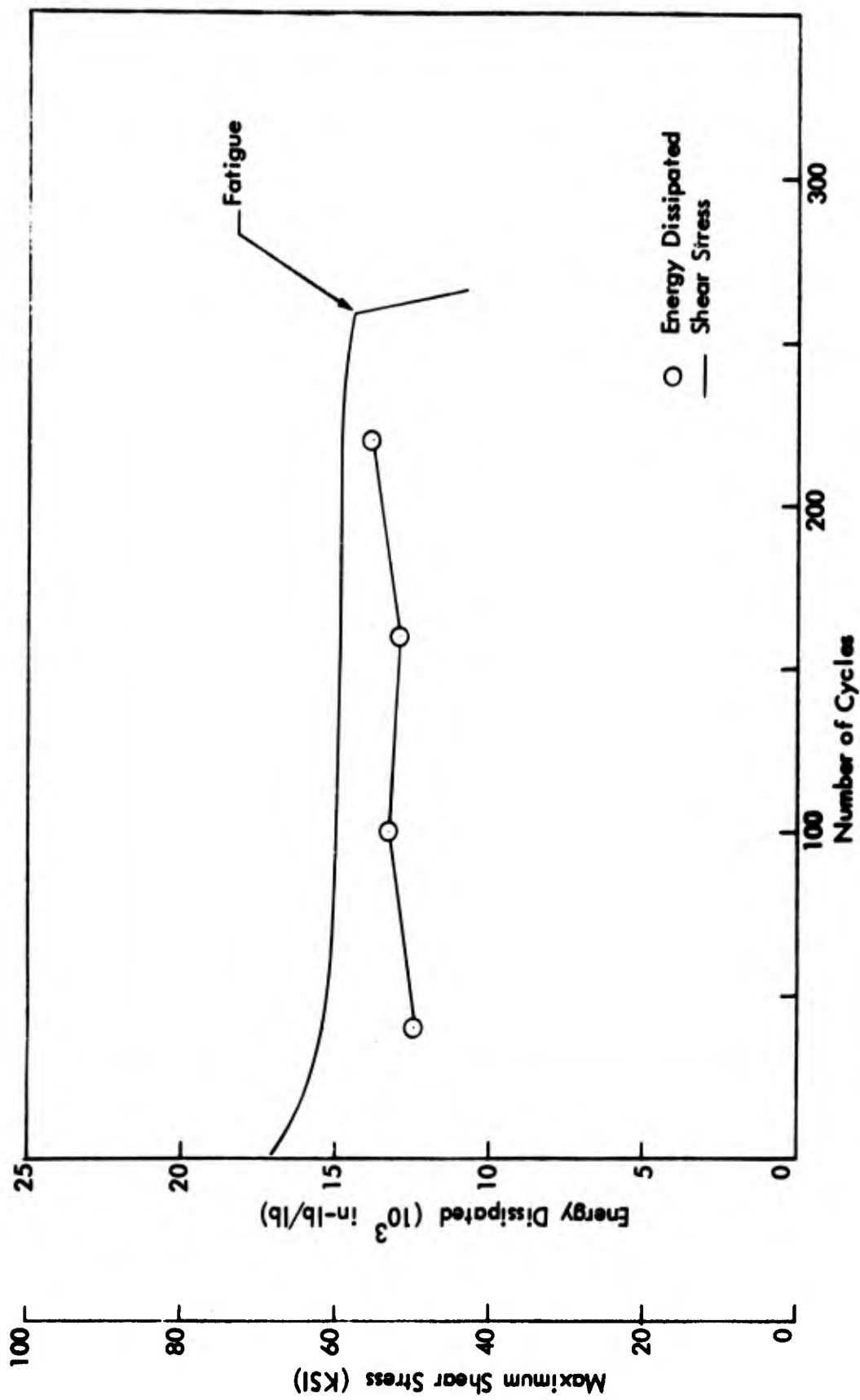


Fig. 24 Typical Changes of Maximum Shear Stress and Energy Dissipated Due to Cyclic Torsion for Beryllium Copper at 3% Total Shear Strain

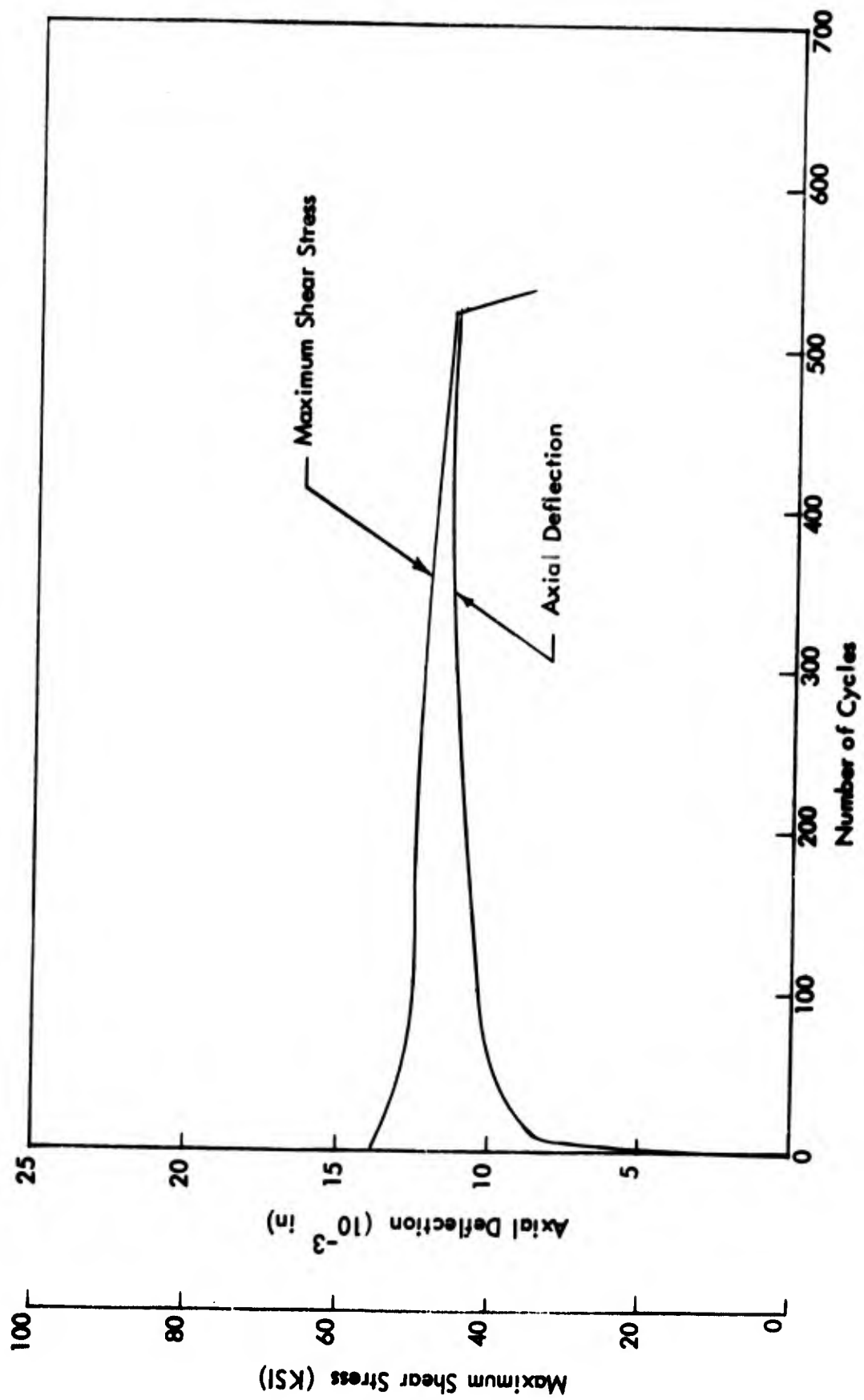


Fig. 25 Typical Changes of Maximum Shear Stress and Axial Deflection Due to Cyclic Torsion for Beryllium Copper at 3% Total Shear Strain and 20,000 psi Axial Compression

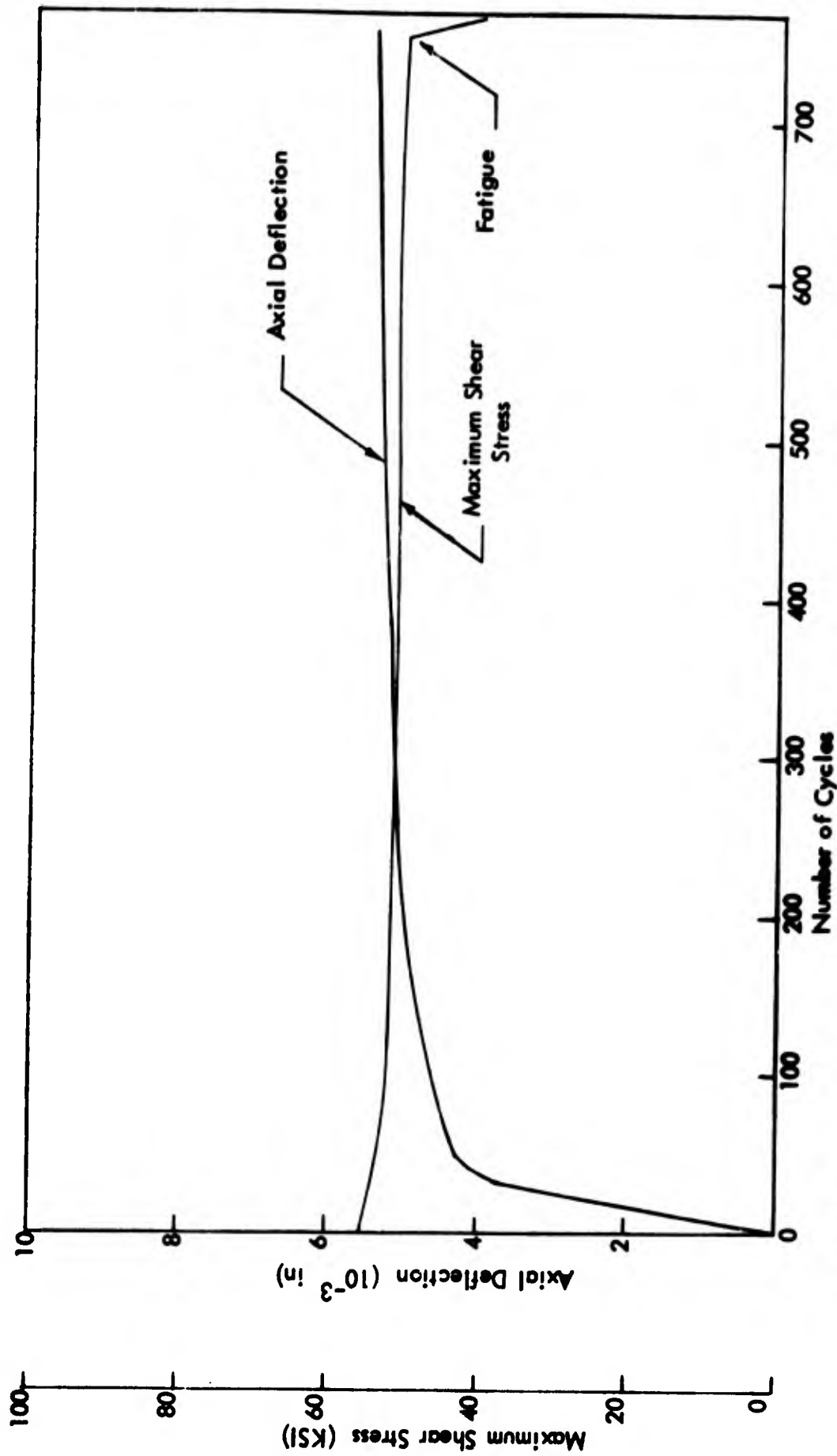


Fig. 26 Typical Changes of Maximum Shear Stress and Axial Deflection Due to Cyclic Torsion for Beryllium Copper at 3% Total Shear Strain and 30,000 psi Axial Compression

translation without change in size or shape and coincides with the plastic potential. However, this axial plastic strain increases at a diminishing rate for beryllium copper. This effect cannot be explained by the kinematic hardening and appears to be due to the fact that the active slip systems have been found to correspond more to the alternate shear stress than to the steady stress.

D. Effect of Cyclic Torsion Strain on Axial Strain

One interesting effect which was experienced by the aluminum alloy Al 2024-T-351 is illustrated in Figures 22 and 23 by comparing the axial deflection data for a 20,000 psi axial compressive stress at 3% and 4% cyclic torsional strain. Comparison of the two axial deflection curves indicate that the axial strain is independent of the cyclic torsion strain at a steady axial compressive load. When additional data becomes available for other materials, the existence of this trend would be interesting

E. Some Analytical Considerations

An empirical stress-strain relation curve for metals was proposed by W. Ramberg and W. R. Osgood¹¹ and is given as follows:

$$\epsilon = \frac{s}{K} + \alpha \left(\frac{s}{K} \right)^r \quad (33)$$

where ϵ is the strain, s is the stress, α is the linearity constant, K is a positive constant, and r is a positive number greater than one. Approximating the cyclic torsional stress-strain relationship by a similar equation, it is found that

$$\Delta \epsilon_p = 2\alpha \Delta \epsilon_e^r \quad (34)$$

where

$$\Delta \epsilon_e = \frac{\tau_{\max}}{G} \quad (35)$$

In the preceding equations, the following additional relationships have been used:

$$\text{total shear strain range: } \epsilon_T = 2\epsilon = 2\Delta\epsilon_e + \Delta\epsilon_p$$

and modulus of rigidity: $G = K$

To find the values of α and γ that give the best fit between equation (34) and experimental data, a logarithmic plot must be made of the plastic strain range $\Delta\epsilon_p$ versus the applied stress τ_{\max} which in turn can be expressed by the elastic strain range $\Delta\epsilon_e$. Thus α and γ are the intercept and the slope of the straight line which best fit the data of this logarithmic plot. The data provided in Figures 27 and 28 illustrate this type of curve fit for aluminum alloy 2024-T4 and beryllium copper. It is found that α and γ for aluminum alloy 2024-T4 are 2.195 and 12.17, respectively. The values of α and γ for beryllium copper are 1.886 and 6.77, respectively.

The test data also indicate that the shape of the hysteresis loop is unchanged. Hence, it can be assumed that the area of the hysteresis loop varies linearly with the plastic strain range, $\Delta\epsilon_p$ and the stress amplitude, τ_{\max} . Therefore, the total energy dissipated in fatigue loading becomes

$$E = C_0 \Delta\epsilon_p \tau_{\max} N \quad (36)$$

where C_0 is a proportional constant. By using Equation (32) and (34), the total dissipated energy can be expressed in terms of plastic strain range $\Delta\epsilon_p$:

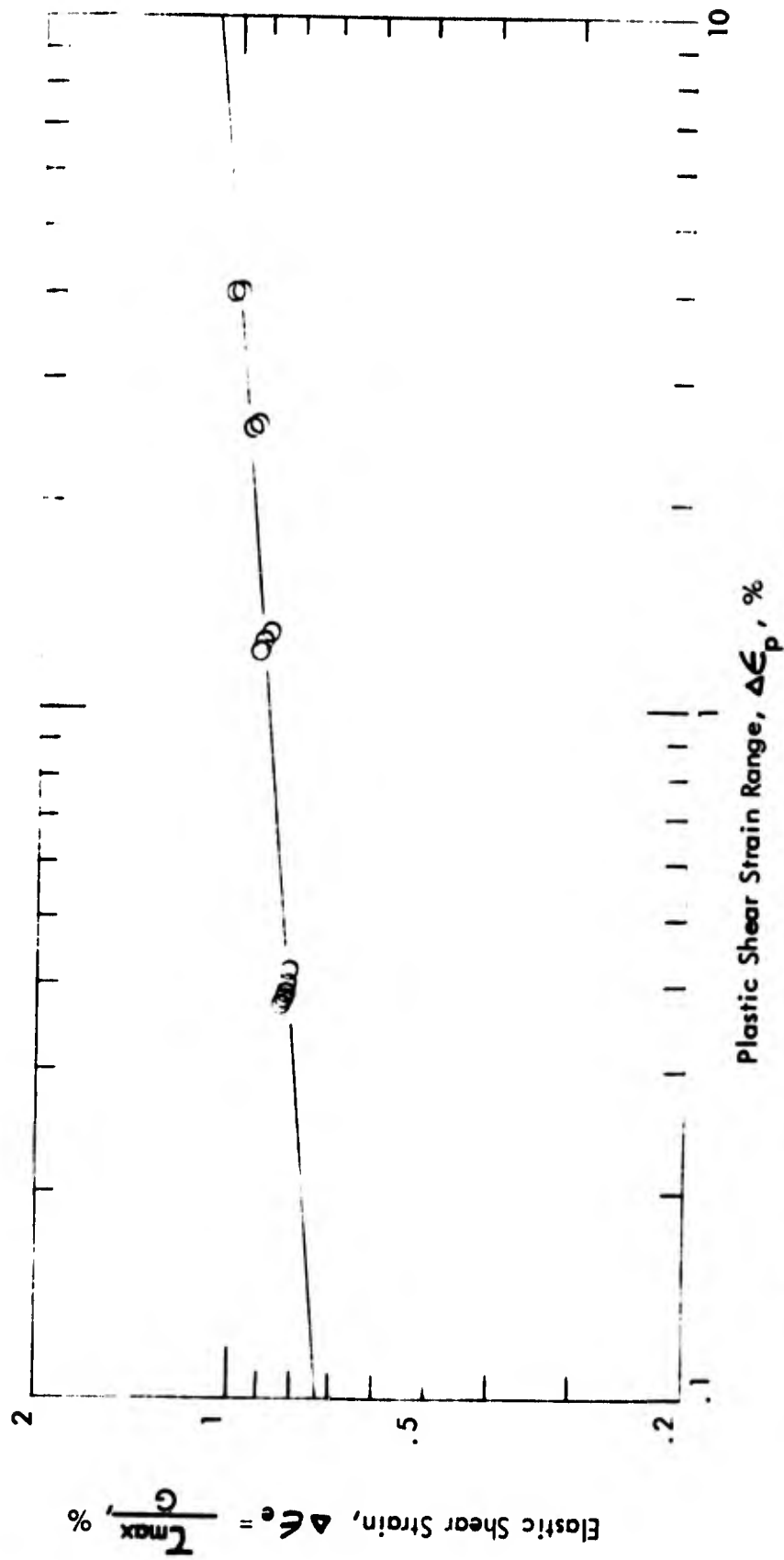


Fig. 27 Variation of Fatigue Stress With Plastic Strain Range
For Al 2024-T4

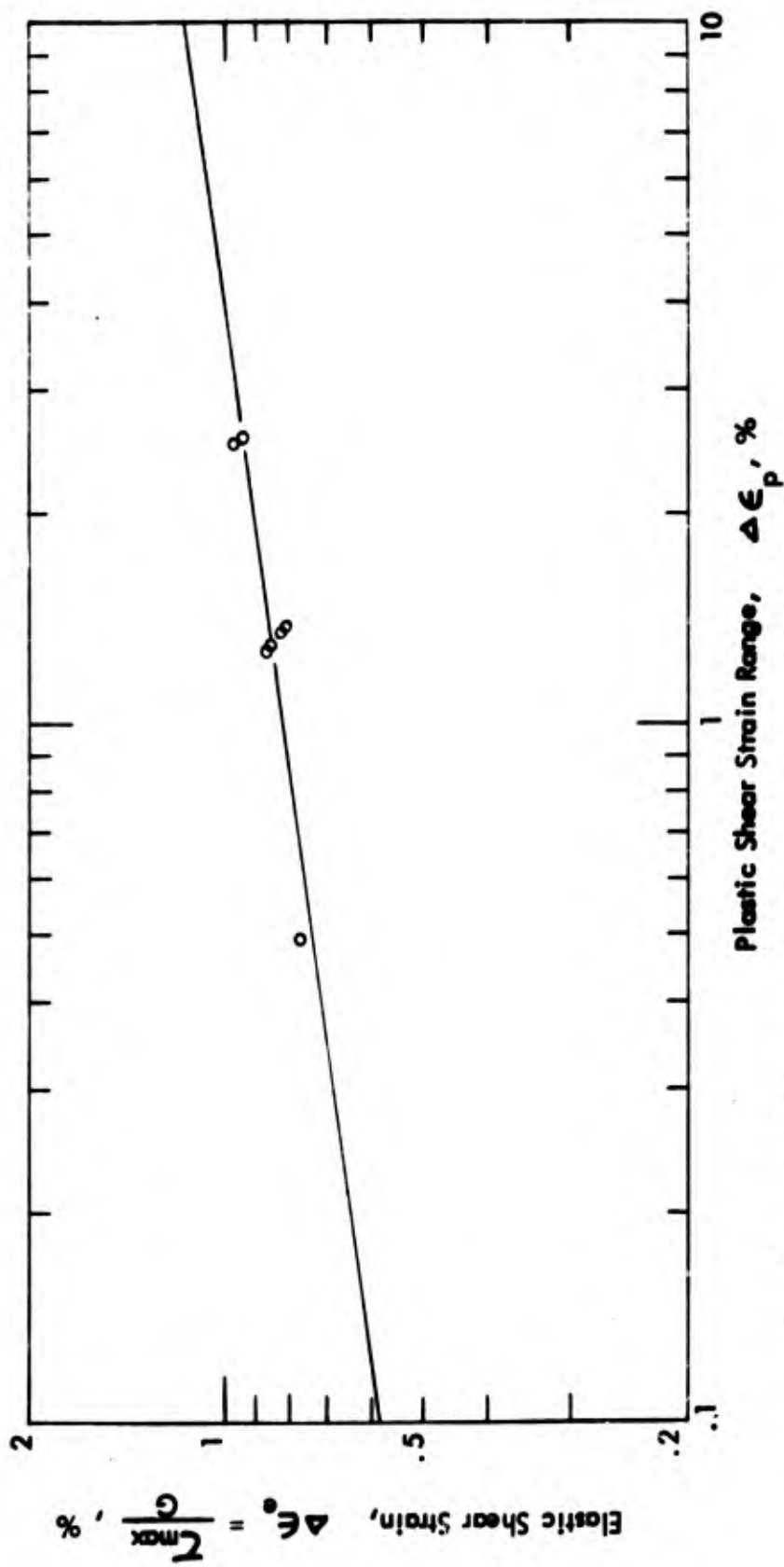


Fig. 28 Variation of Fatigue Stress With Plastic Strain Range For Beryllium Copper

$$E = C_E \Delta \epsilon_p \left[1 + \frac{1}{\delta} - \frac{1}{m} \right] \quad (37)$$

where C_E is a constant. If a logarithmic plot is made of the total dissipated energy versus the plastic strain range, then the slope of the straight line which fits best the test data must be equal to $1 + \frac{1}{\delta} - \frac{1}{m}$. In other words, with the slope of $1 + \frac{1}{\delta} - \frac{1}{m}$, a straight line can be found, which fits best the test results. Then the constant C_E is given by the value of total energy at $\Delta \epsilon_p = 1\%$. Figure 29 shows that this logarithmic energy plot for aluminum alloy 2024-T4 with a straight line slope of $1 + \frac{1}{\delta} - \frac{1}{m} = -0.3313$ best fits the test data. From this plot, the constant C_E is found to be 1.758×10^6 . Hence, a semi-empirical energy formula for aluminum 2024-T4 has been obtained and is provided as follows:

$$E = 1.758 \times 10^6 \Delta \epsilon_p^{-.3313}$$

where E is in in-lb/lb and $\Delta \epsilon_p$ in percent.

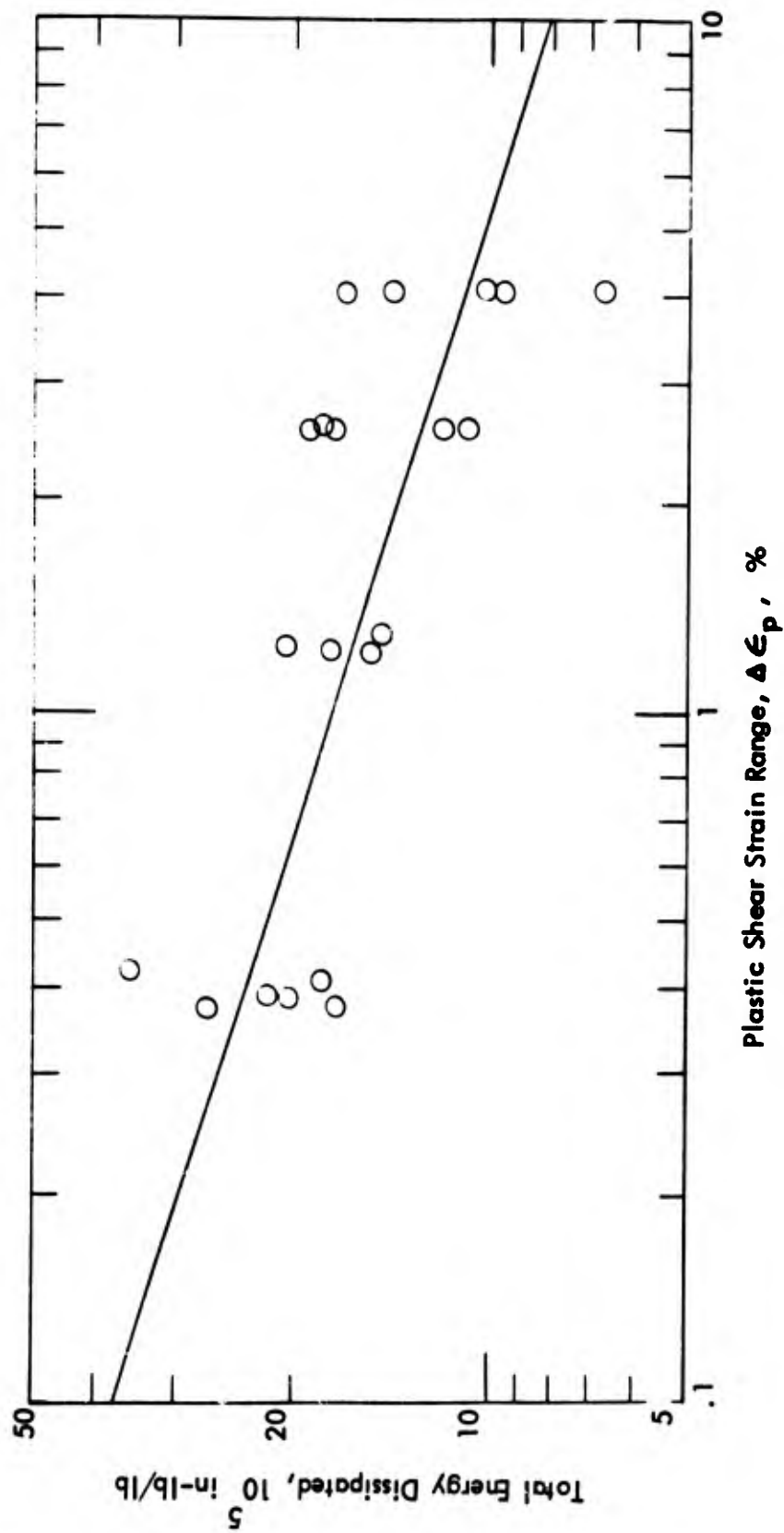


Fig. 29 Variation of Total Energy Dissipated Due to Cyclic Torsion With Plastic Strain Range For Aluminum Alloy 2024-T4

VI REFERENCES

1. Timoshenko, S. and Woinowsky, S., Krieger, "Theory of Plates and Shells", McGraw Hill Book Co., p. 48, 1959.
2. Von Karman, Th., "Encyklopadie der Mathematischen Wissenschaften", Vol. IV₄, p. 349, 1910.
3. Mansfield, E. H. and Kleeman, P. N., "A Large Deflection Theory for Thin Plates", Aircraft Engineering, Vol. 27, p. 102, 1955.
4. Mansfield, E. H., "The Inextensional Theory for Thin Flat Plates", Quart. J. Mech. App. Math., Vol. 8, p. 338, 1955.
5. Platus, D. L., et al, "Concepts of Multiple-Impact Study of Energy Absorption", Final Report, Contract NAS 7-226, ARA Report #49, Oct. 1964.
6. Forrest, P. G., "Fatigue of Metals", Addison Wesley Publishing Co., Inc., pp 107 - 113, 1963.
7. Coffin, L. F., Jr., "Cyclic Straining and Fatigue" in Internal Stresses and Fatigue in Metals edited by G. M. Rossaliles and W. L. Gunbe, published by Elaevier Publishing Co., pp 363 - 381, 1959.
8. Thompson, N. and N. J. Wadsworth, "Metal Fatigue", Advances in Physics, Vol. 7, No. 25, 1958.
9. Lin, T. H. and Ito, M., "Theoretical Plastic Distortion of a Polycrystalline Aggregate Under Combined and Reversed Stresses", J. Mech. Phys. Solids, Vol. 13, pp 103 - 115, 1965.
10. Drager, W., "The Theory of Plasticity", A Survey of Recent Achievements, Proc. Inst. Mech. Engrs. London, p. 169, 1955.
11. Ramberg, W., and Osgood, W. R., "Description of Stress-Strain Curves by Three Parameters", NACA TN 902, July 1943.

UNCLASSIFIED

Security Classification

DOCUMENT CONTROL DATA - R & D

(Security classification of title, body of abstract and indexing annotation must be entered when the overall report is classified)

1. ORIGINATING ACTIVITY (Corporate author) Aerospace Research Associates, Inc. 2017 West Garvey Avenue West Covina, California 91790		2a. REPORT SECURITY CLASSIFICATION UNCLASSIFIED	
		2b. GROUP	
3. REPORT TITLE RESEARCH ON ENERGY ABSORBING STRUCTURES, PART VI			
4. DESCRIPTIVE NOTES (Type of report and inclusive dates) Scientific Interim			
5. AUTHOR(S) (First name, middle initial, last name) Bernard Mazelsky T H Lin Sheng-Rong Lin			
6. REPORT DATE March 1968	7a. TOTAL NO. OF PAGES 68	7b. NO. OF REFS 11	
8a. CONTRACT OR GRANT NO. AF 49(638)-1521	8b. ORIGINATOR'S REPORT NUMBER(S) ARA Report No. 94		
8c. PROJECT NO. 9782-01	9b. OTHER REPORT NO(S) (Any other numbers that may be assigned this report) AFOSR - 68 - 0489		
8d. 6144501F			
8e. 681307			
10. DISTRIBUTION STATEMENT 1. Distribution of this document is unlimited.			
11. SUPPLEMENTARY NOTES TECH, OTHER		12. SPONSORING MILITARY ACTIVITY AF Office of Scientific Research (SREM) 1400 Wilson Boulevard Arlington, Virginia 22209	
13. ABSTRACT An analytical method for predicting very large deflections of flat rectangular plates subjected to non-symmetric loads, with respect to the centerline of the flat plate, has been developed and correlated with experiment. For deflections below twenty percent of the plate's length and/or width, the theory of Mansfield and Kleeman's could be used. For large deflections and loading conditions, their theory is inapplicable due to the change in moment arm caused by the plate's deflection. The present theory properly accounts for the moment arm correction for plate deflections up to sixty percent of its length and/or width. An extensive experimental study was made on low cycle fatigue of thin walled specimens. The total energy absorbed in cyclic torsion for two types of aluminum A-1100 and 2024 T-3 were measured. The 2024 aluminum has 4 to 5 times the energy absorption capability of the A-1100 aluminum. Axial compressive stress on cyclic torsion of beryllium copper increased the total energy absorption 3 to 4 times as that when no compressive axial stress was applied. The large deflection theory was applied to the successful design and manufacture of an energy absorbing highway protective barrier system for the Department of Transportation.			

DD FORM 1473
1 NOV 64

UNCLASSIFIED

Security Classification

UNCLASSIFIED

Security Classification

KEY WORDS	LINK A		LINK B		LINK C	
	ROLE	WT	ROLE	WT	ROLE	WT
Energy Absorbing Structures						
Large Deflection Theory						
Large Deflections of Plates and Shells						

UNCLASSIFIED

Security Classification